MNRAS **000**, 1–?? (2017) Preprint 30 May 2022 Compiled using MNRAS LATEX style file v3.0

MASCOT: Molecular gas depletion times and metallicity gradients - evidence for feedback in quenching active galaxies

Caroline Bertemes,[1] ★ Dominika Wylezalek, [1]
[1] *Zentrum für Astronomie der Universität Heidelberg, Astronomisches Rechen-Institut Mönchhofstr, 12-14 69120 Heidelberg, Germany*

Accepted XXX. Received YYY; in original form ZZZ

ABSTRACT

We present results from the first public data release of the MaNGA-ARO Survey of CO Targets (MASCOT; Wylezalek et al. 2022) survey. Focusing on the regime below the star-forming Main Sequence, we find an empirical relation between gas-phase metallicity gradients ∇Z and global molecular gas depletion times $t_{\rm dep}$ in optically-selected type 2 AGN/LINERs/Composites with "more quenched" systems showing flatter/positive gradients. Our results are based on the O3N2 metallicity diagnostic given that it was recently suggested to be robust w.r.t DIG and LI(N)ER emission. We conduct a systematic investigation into possible drivers of the observed $\nabla Z - t_{\rm dep}$ relation (ouflows, gas accretion, in-situ star formation, mergers, and morphology). In our sample of AGN, LINERs and Composites, we find a strong relation between ∇Z and the median [O III] velocity broadening within 1 R_e, as well as signatures of suppressed star-formation in the outskirts at long $t_{\rm dep}$ using a full spectral fitting procedure. We find no evidence of inflows impacting the metallicity gradients, nor of our results being significantly affected by merger activity or morphology. We thus conclude that the observed $\nabla Z - t_{\rm dep}$ relation may stem from combination of metal distribution via weak feedback, and connection to in-situ star formation via a resolved mass-metallicity-SFR relation.

1 INTRODUCTION

One of the key goals in galaxy evolution is to quantify the growth of galaxies, which occurs via the conversion of gas into stars. Specifically, the fuel for star formation is held in the form of a cold, molecular gas phase, which fragments and contracts via cooling until a critical density is reached and gravitational collapse ensues, culminating in the ignition of nuclear fusion and thus the birth of new stars (e.g. Schmidt 1959; Kennicutt 1998). During the actively star-forming phase in the lives of galaxies, their growth has further been observed to follow a tight relation between the rate of star formation SFR and the stellar mass $M_\star$ already in place. This relation is known as the Main Sequence (MS; Brinchmann et al. 2004; Noeske et al. 2007). The star-forming branch around the MS can be contrasted to the cloud of passive galaxies, and their ensemble forms a bimodal distribution in the SFR-$M_\star$ plane. The regime in between both populations, dubbed the Green Valley, is sparsely populated, which has been suggested to point to rapid quenching as galaxies transition from the star-forming into the passive regime towards the end of their life (see Salim 2014 for a review).

Studies of the cold neutral gas phase hold important clues for characterising and understanding SFR fluctuations and the quenching of galaxies, and thus represent a prime element in compiling a theory of galaxy evolution. For instance, it has been shown that galaxies below the Main Sequence are not only more devoid of molecular gas, but also less efficient at converting their remaining gas into stars (e.g. Saintonge et al. 2017; see also Saintonge & Catinella 2022 for a detailed review). The recent rise of state-of-the-art integral field unit (IFU) and multi-object spectroscopy (MOS) facilities enables studies to go beyond investigating how molecular gas properties shape galaxies in a global way by resolving galaxies as extended dynamic systems. For instance, the EDGE-CALIFA (Extragalactic Database for Galaxy Evolution - Calar Alto Integral Field Area survey; Bolatto et al. 2017) and ALMaQUEST surveys (ALMA-MaNGA QUEnching and STar formation; Lin et al. 2020) have conducted resolved CO radio observations on samples of galaxies with optical-IFU data. The EDGE-CALIFA collaboration conducted CO follow-up observations of 177 galaxies with existing CALIFA data with the CARMA (Combined Array for Millimeter-wave Astronomy) interferometer, which will further be expanded by ongoing observations with the APEX telescope (295 targets to date; Colombo et al. 2020). The goal of this survey is to study the resolved relationships between molecular gas and e.g. stellar mass and SFR, ionised gas kinematics, dust extinction, as well as physical and chemical conditions within galaxies. For instance, Colombo et al. (2020) recently found evidence for a scenario in which the quenching of galaxies starts with an initial central shortage of molecular gas, but that in a second phase a decrease in star forming efficiency becomes the most important driver for permanently pushing galaxies into quiescence. The ALMaQUEST survey operates at similar scales of $\sim$ 1 kpc, and is based on Atacama Large Millimeter Array (ALMA) CO observations of galaxies with existing optical 3D data from MaNGA (Mapping Nearby Galaxies at Apache Point Observatory; Bundy et al. 2015). Their sample of 46 galaxies was selected to cover a wide range in star-forming regimes, from starbursts down to CO-fainter Green Valley galaxies. Starbursts within ALMaQUEST were shown to be primarily driven by an increased star-forming efficiency (Ellison et al. 2020), while Green Valley galaxies show both suppressed star-forming efficiencies and molecular gas fractions w.r.t the MS, both in star-forming as well as 'retired' spaxels (Lin et al. 2022).

Complementary the ALMaQUEST and EDGE-CALIFA survey, we recently published the first data release of our MaNGA-ARO Survey of CO Targets (MASCOT; Wylezalek et al. 2022). Using 12m single-dish ^{12}CO(1-0) observations with the Arizona Radio Observatory, we have collected data for 187 MaNGA galaxies to date, selected to span a broad range in stellar masses ($\sim$ 1.5 dex) and sSFR = SFR/M$_\star$ ($>$ 3 dex), thus enhancing the number statistics of galaxies with simultaneously available optical-IFU data and (galaxy-integrated) CO observations. Further observations are still ongoing. We note that MASCOT is highly complementary to ALMaQUEST in terms of the field of view probed by the CO observations (while drawing from the identical underlying optical-IFU survey), and therefore we include the public global ALMaQUEST data in Wylezalek et al. (2022) together with the MASCOT DR1 for convenience.

In this paper, we present first results based on the first data release. In particular, we combine the study of molecular gas properties with resolved metallicities and kinematics, as the latter are, amongst others, sensitive to gas accretion, feedback mechanisms and in-situ star formation. We also investigate to what extent inflows/outflows have any measurable impact on star formation via influencing the availability of fuel, or its consumption.

The above-mentioned studies are of particular interest in the regime below the Main Sequence, including the Green Valley, to uncover information about the drivers of quenching. However, (resolved) metallicity studies have traditionally been sparse in the below-MS regime given the prevalence of diffuse ionised gas (DIG) contamination. To investigate to what extent DIG emission as well as low-ionization (nuclear) emission-line regions (LINERs/LIERs) may or may not bias strong line metallicity calibrators, Kumari et al. (2019) studied individual DIG/LI(N)ER - HII region pairs in nearby galaxies with archival Multi Unit Spectroscopic Explorer (MUSE) data resolving 50 – 100 pc scales. Identifying those pairs sufficiently close to each other to share the same metallicity, they encouragingly found the O3N2 diagnostic (based on Hα, [N III] λ6583, Hβ, and [O III] λ5007) to be remarkably robust in DIG/LI(N)ER regions. Motivated by these findings (summarised in more detail in Section 3.1 along with additional observational studies), we therefore focus on the below-MS regime in this work, using the O3N2 diagnostic to study the interplay between metallicity gradients and molecular gas properties, and furthermore include LI(N)ERs and Composites in our analysis.

The paper is organised as follows: In Section 2, we describe the data products we use, including a more detailed description of the MASCOT observations. In Section 3, we outline the sample selection and present the main focus of this paper, namely a relation found between metallicity gradients ∇Z and molecular gas depletion time $t_{\rm dep}$ within AGN, LINERs and Composites below the MS, while also performing sanity checks about the robustness of this relation. In Section 4, we expand our data analysis by investigating the viability of several possible drivers behind the $\nabla Z - t_{\rm dep}$ relation: gas flows, in-situ star formation, mergers and morphology. Finally, we proceed to summarise our findings in Section 5. Throughout this paper, we assume a standard cosmology with $H_0 = 70\,{\rm km\,s^{-1}}\,Mpc^{-1}$, $\Omega_m = 0.3$ and $\Omega_\Lambda = 0.7$.

2 DATA

2.1 MASCOT

Our primary dataset is the MaNGA-ARO Survey of CO Targets (MASCOT; first data release presented in Wylezalek et al. 2022). MASCOT is an ESO Public Spectroscopic Survey using the Arizona Radio Observatory (ARO) to conduct single-dish CO(1-0) follow-up observations of galaxies with existing optical-IFU data from the Mapping Nearby Galaxies at Apache Point Observatory (MaNGA) survey, which will be summarised below in Section 2.3. The main objective of MASCOT is to investigate the relation between molecular gas properties and spatially resolved optically-derived quantities. In particular, the size of the sample (consisting to $\sim$ 20% of AGN/LINERs/Composites) enables us to investigate how such relations vary for galaxies with different levels of star-forming and AGN activity, and examine the role of morphology and environment.

Observations were carried out using the 3mm receiver on the 12m ARO antenna (equivalent to ALMA Band 3, 84 – 116 GHz). To inform our observing strategy, we performed on-the-fly data reduction and stayed on-target until we either obtained a detection at the level of $\gtrsim 5\sigma$, reached a sensitivity limit of rms = 0.25 mK (using velocity bins of $\sim$ 50km/s), reached the end of a given observing block, or the telescope required a point-focus. Moreover, we prioritised targets according to their visibility (i.e. low air masses), whilst avoiding to point the antenna directly into the Sun or the wind. Besides visibility considerations, our sample was further designed to span a broad range in stellar masses $\log M_\star > 9.5 M_\odot$ and specific SFRs focused around the Main Sequence, as well as including a number of Green Valley galaxies and starbursts. In more detail, the first data release consists of 187 galaxies spanning over 1.5 dex in stellar mass and over 3 orders of magnitude in sSFR. Fig 1 shows the position of our targets in the MS plane, supplemented by the ALMaQUEST survey (see Section 2.2 below). The dashed line shows the local MS relation obtained by Renzini & Peng (2015). In this work, we focus on the below-MS regime and thus exclude all galaxies above the dashed line. Our sample contains inactive galaxies, as well as LINERs/Composites and Seyfert AGN, which are coloured in green, purple and black, respectively, according to a Baldwin et al. (1981) classification within the central 1 kpc (discussed in more detail in Section 3.1).

We provide the binned and unbinned CO profiles, along with other raw data products (e.g. CO fluxes and luminosities) and derived quantities (e.g. H_2 masses and kinematics of the fitted CO lines), on the MASCOT website [1]. The H_2 masses are derived using the $\alpha_{\rm CO}$ conversion factor from Accurso et al. (2017) which depends on metallicity, as well as offset in SFR from the star-forming Main Sequence relation (which we take from Renzini & Peng 2015). The first data release of MASCOT makes use of e.g. the stellar masses and SFRs from the Pipe3D catalog (Sánchez et al. 2016, 2018; described in more detail in Section 2.3.2) to calculate molecular gas fractions and depletion times. While the Accurso et al. (2017) $\alpha_{\rm CO}$ conversion was established based on the Pettini & Pagel (2004) calibrator, metallicities based thereupon are not included in the Pipe3D catalog. Wylezalek et al. (2022) therefore uses the Pipe3D oxygen abundances based on the Maiolino et al. (2008) prescription, and corrects for a constant offset of 0.05 w.r.t Pettini & Pagel (2004) metallicities within our mass range (Sánchez et al. 2017). In this work, we use the same metallicity-dependent H_2 masses for consistency, but we verify that our conclusion would not be strongly affected when using a constant $\alpha_{\rm CO}$ conversion factor independent of metallicity instead (Section 3.3).

[1] https://wwwstaff.ari.uni-heidelberg.de/dwylezalek/mascot.html

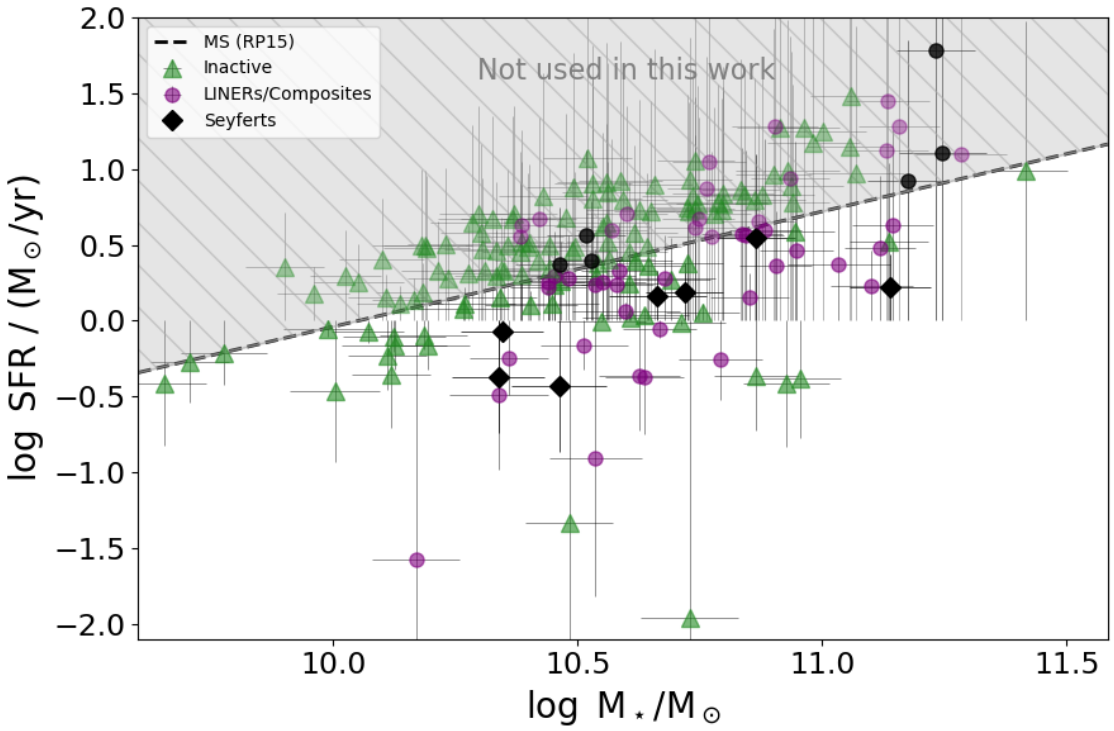

Figure 1. Location of the MASCOT sample within the plane of star formation rate SFR versus stellar mass $M_\star$. The Renzini & Peng (2015) Main Sequence (MS) relation is shown as a dashed line. In this work, we focus on the below-MS regime and thus discard the targets above the line as illustrated by the grey hatched region. The green datapoints correspond to inactive galaxies, the purple ones to LINERs and Composites, and the black ones to Seyfert AGN, according to a Baldwin et al. (1981) classification based on their central kpc.

2.2 ALMaQUEST

We are supplementing our ARO CO(1-0) observations with data from the ALMA-MaNGA QUEnching and STar formation survey(ALMaQUEST; Lin et al. 2020). The ALMaQUEST project used the Atacama Large Millimeter Array (ALMA) to perform spatially resolved CO(1-0) follow-up observations of 46 galaxies included in the MaNGA survey (described in Section 2.3 below) with a broad range of star-forming activity ranging from starbursts to Green Valley galaxies. The field-of-view in the chosen ALMA configuration is ∼ 50", broadly similar to the ARO beam size of ∼ 55" used in our MASCOT observations. Galaxy-integrated measurements from ALMaQUEST are included in Wylezalek et al. (2022) along with the first MASCOT data release .

2.3 MaNGA

As mentioned above, the science goal of the MASCOT survey (Section 2.1) is to study the connection between resolved optically-derived galaxy parameters and molecular gas properties via CO(1-0) observations. The required optical-IFU data is taken from the public Mapping Nearby Galaxies at Apache Point Observatory (MaNGA) survey, which constitutes the underlying population from which the MASCOT sample is drawn. We now proceed to describe the MaNGA survey and relevant data products in more detail.

2.3.1 MaNGA survey overview

The Mapping Nearby Galaxies at Apache Point Observatory (MaNGA) survey (Bundy et al. 2015) is part of the fourth generation of the Sloan Digital Sky Survey (SDSS; Blanton et al. 2017). Launched in July 2014, MaNGA has been collecting optical-IFU spectra for ∼ 10k galaxies at low redshift ($\langle z \rangle \sim 0.03$) using the two BOSS (Baryonic Oscillation Spectroscopic Survey) spectrographs mounted on the 2.5 metre Sloan telescope at the Apache Point Observatory (APO). The red and blue arm of the BOSS spectrographs cover the wavelength range from 3600 Å to 10300 Å (Smee et al. 2013), with a median spectral resolution $\langle R \rangle \sim 2000$. The MaNGA sample is designed to to follow a roughly flat distribution in log $M_\star$ above $10^9 M_\odot$ (Wake et al. 2017), with about two third of the targets being observed out to 1.5 R_e ("primary" sample) and the rest being covered out to 2.5 R_e ("secondary" sample). We refer the reader to Law et al. (2015) and Yan et al. (2016a,b) for details on the observational strategy and Data Reduction Pipeline (DRP). The final DRP datacube products are interpolated on a grid of 0.5" x 0.5" spaxels, corresponding to roughly 1 – 2 kpc (while the effective angular resolution amounts to ∼ 2.5").

2.3.2 Pipe3D measurements

In this work, we make use of the public Pipe3D Value Added Catalog (Sánchez et al. 2016, 2018). This dataset contains estimates of key galaxy properties - including stellar population properties, star formation histories, emission line models and stellar absorption indices - as recovered by running the Pipe3D full spectral fitting pipeline using the spectra of MaNGA galaxies on a spaxel-by-spaxel basis. Pipe3D is an iterative MCMC-based fitting procedure, which derives the best-fit stellar velocity and velocity dispersion fields in a first step, then proceeds to constrain the amount of dust attenua-

tion with fixed stellar kinematics in a second iteration. The results from these first two steps are then used to fit the continuum as a linear combination of simple stellar population (SSP) templates to recover galaxy quantities, while independently modelling the emission lines with multiple Gaussians. The adopted stellar library combines GRANADA theoretical stellar templates (Martins et al. 2005) with the MILES stellar library (Sánchez-Blázquez et al. 2006; Vazdekis et al. 2010; Falcón-Barroso et al. 2011).

In this work, we will use the Pipes3D integrated stellar mass, SFR as well as metallicities and gradients thereof. For our choice of metallicity calibrator, we maintain consistency with Wylezalek et al. (2022) presenting the MASCOT survey and use the Pipe3D oxygen abundances at $1R_e$ based on the Maiolino et al. (2008) prescription ("oh_re_fit_m08"; M08). As we derive H_2 masses using the metallicity-dependent conversion from Accurso et al. (2017) and as those authors used the O3N2 prescription from Pettini & Pagel (2004), we apply a correction of +0.05 dex to the Pipe3D M08 metallicities to account for the offset. However, for the metallicity *gradients*, we follow a slightly different approach. In this work, motivated by the results in Kumari et al. (2019) which found the O3N2 diagnostic to be reasonably robust in DIG and LI(N)ER regions with a scatter of 0.05 dex (see also Section 3.1), we are investigating metallicity gradients below the Main Sequence where DIG levels are elevated. We therefore choose to use directly the Pipe3D oxygen abundance gradient based on the O3N2 calibrator from Marino et al. (2013) ("alpha_oh_re_fit_o3n2") evaluated within $0.5 - 2\ R_e$. We will further conduct a sanity check where we instead use the Pipe3D gradients based on the Tremonti et al. (2004) calibrator which uses the R23 ratio, as the latter has been shown to be less sensitive to ionisation (Kewley et al. 2019; Fig 9), at least within the metallicity range of our dataset.

2.3.3 *Radially resolved full spectral fitting procedure*

We carry out a radially resolved full spectral fitting procedure to incorporate the possible impact of the star formation distribution and resolved stellar masses in our analysis. Our approach follows the stellar population synthesis (SPS) method, in which a given spectrum is fitted as a superposition of the emissions from stellar populations of different ages and metallicities. We run our fitting procedure on radial spectra, obtained by dividing each galaxy into annuli of $0.2\ R_e$ width tracing the elliptical Petrosian apertures, and apply aperture corrections to recover the total g-band flux from the NASA-Sloan Atlas catalog (NSA; Blanton et al. 2011).

While we defer a detailed description of our fitting procedure to an upcoming paper (Bertemes et al. 2022), it can be briefly summarised as follows: We use the Bagpipes code (Carnall et al. 2018) to model the observed emission in galactic annuli via a superposition of stellar populations following a 2-component star formation history (SFH) consisting of a lognormal and a decoupled recent burst of constant SFR operating over the past 30 Myr. Each of the two SFH components assumes a single stellar metallicity for all of its stars (which for the recent burst corresponds to the gas-phase metallicity). Bagpipes is based on the 2016 version of the Bruzual & Charlot (2003) models, and assumes a Kroupa & Boily (2002) IMF. We simultaneuously fit the MaNGA spectra and associated NSA photometry in the optical wavelength range of 3700 – 7400 Å, assuming a Calzetti et al. (2000) extinction law. We further assume a fixed ratio of nebular to stellar attenuation $\eta = 1/0.44$ due to birthcloud dust, as also retrieved by Calzetti et al. (2000). Ionised gas emission lines are modelled self-consistently in Bagpipes with CLOUDY (Ferland et al. 1998). However, we mask the [O II] λ3726, 3729 and [S II] λ6716, 6731 lines, as it was found empirically that they were challenging to reproduce simultaneously with the Balmer lines, [O III] λ5007, and [N III] λ6583, which we prioritise as they hold significant information about the SFR as well as physical and chemical conditions in the ISM. We attribute this challenge to the relatively simplified CLOUDY photoionisation model grid used in terms of assumptions about e.g. the birthcloud age, metallicity, and ionisation parameter. Further, we introduce more freedom to the H_α line fitting via a normalisation parameter allowed to vary between 1 – 1.5. The rationale behind this parameter is that at fixed SFR, the Hα luminosity predicted by Bagpipes (based on its underlying CLOUDY grid) is known to feature a a systematic offset w.r.t to the values predicted by Kennicutt of up to 0.2 dex depending on metallicity and ionisation. Moreover, we set a logarithmic prior on the time of peak star formation, which was found to be required for consistency with the cosmic SFR density in the photometric fitting runs in Carnall et al. (2019). Finally, we impose a prior following a student's t-distribution on the jump in SFR between the recent burst and the early SFH, which will favour a smooth transition in the absence of constraining information (Leja et al. 2019).

We find that when running our fitting procedure on our sample defined in Section 3.1 below, our recovered global SFRs agree well with the Pipe3D measurements, with only a minor offset of 0.12 dex and a scatter of 0.19 dex. Similarly, our recovered stellar masses are offset from the Pipe3D reference values by < 0.001 dex, with a scatter of ~ 0.13 dex.

3 ANALYSIS

3.1 Sample selection and choice of metallicity calibrator

In this work, we are are focusing on the interplay between resolved metallicities and molecular gas properties in galaxies that are located *below the Main Sequence (MS)*. Metallicity studies have traditionally been sparse in this regime due to the ubiquity of diffuse ionised gas (DIG) regions, and concerns about the latter potentially contaminating common metallicity diagnostics. It has been suggested that DIG emission may bias strong line diagnostics by contributing to the line fluxes entering the calculation (Zhang et al. 2017). Recently, in this context, Kumari et al. (2019) established a metallicity prescription for DIG- and LI(N)ER-dominated regions. Exploiting Multi Unit Spectroscopic Explorer (MUSE) observations at 50−100 pc scale resolution in 24 nearby star-forming galaxies, the authors selected a sample of individual DIG/LI(N)ER - HII region pairs located sufficiently close to each other to be assumed to share a single metallicity. In particular, the study encouragingly found the O3N2 diagnostic (based on Hα, [N III] λ6583, Hβ, and [O III] λ5007) to be remarkably robust in DIG/LI(N)ER regions, showing only a minor offset of < 0.04 dex from the ground truth with 0.05 dex scatter. Seyfert-classified spaxels located in the outskirts were also included in the analysis. On the topic of possible DIG contamination, a similar conclusion was reached by Vale Asari et al. (2019) for a set of $\sim$ 1400 MaNGA galaxies, with the additional challenge that the ~kpc scale resolution does not allow resolving individual HII regions. The authors used high-S/N star-forming spaxels and characterised the contribution of DIG to relevant emission lines via the Hα line, concluding that the O3N2 metric was not significantly affected by DIG contamination (while a moderate impact was recovered for [N II]/ Hα). On the other hand, a study by Zhang et al. (2017) analysed 365 face-on star-forming MaNGA galaxies

(facing as well the challenge of the ∼kpc scale spatial resolution), and found the O3N2 index to be biased in DIG-dominated regions of low surface brightness density. However, they found the associated bias in O3N2-based metallicity gradients to be limited to ± 0.05 dex$/R_e$ in either direction. Given the symmetric character of the bias, one can argue that given sufficient number statistics, any DIG contamination could thus not cause any artificial correlations of the gas-phase metallicity gradient with other galaxy properties, but merely weaken any existing trends at worst. All things considered, these results reinforce our confidence in applying the O3N2 metallicity diagnostic (taken from the Pipe3D catalog as discussed in Section 2.3.2) to galaxies showing DIG emission. Further, while observational studies investigating the impact of LI(N)ER emission on different metallicity calibrators are still sparse to date, the above-mentioned results of Kumari et al. (2019) motivate us to explore O3N2-derived metallicity gradients within the LINERs, Seyferts and Composites in the MASCOT sample as well. In light of these considerations, we select a below-MS sample as follows:

- We start by using the Renzini & Peng (2015) Main Sequence prescription to select all targets from the MASCOT (+ALMaQUEST) sample that fall below the relation.
- Among these, we exclude edge-on galaxies with $b/a < 0.2$
- We exclude type I AGN using the Comerford et al. (2020) catalog as host galaxy properties are challenging to derive in cases where the central QSO outshines its host.
- We further exclude major mergers identified by visual inspection. In galaxies undergoing a major merger with disturbed morphology, radial profile analyses are complicated by the fact that spaxels at the same distance from the centre may not be directly comparable to each other if the galaxy is disrupted in a non-axisymmetric way. Mergers may moreover affect the metallicity distribution within galaxies via mixing processes and inflows, as we will discuss in more detail in Section 4.4. In our radial metallicity gradient study, it is therefore preferable to not include mergers in the same category as isolated galaxies.
- Finally, we split our sample to consider separately purely star-forming galaxies and "AGN-like" objects which include LINERs, Composites and Seyferts. The latter are identified via the NII and SII BPT diagram (Kewley et al. 2001; Kauffmann et al. 2003) using the line ratios extracted from a circular aperture of 1 kpc around the centre. For spaxels that fall only partially within the circle, we use as weights the fraction of their area which belongs to the circle. We further exclude spaxels that are flagged as unusable by the MaNGA DAP ("DONOTUSE" flag[2]), as well as those with S/N< 3 for any of the BPT lines or with negative line fluxes. Finally, we follow Sánchez et al. (2018) by requiring AGN-like objects to have an Hα equivalent width above 1.5 Å. The methodology will be further detailed in an upcoming paper (Alban et al. 2022).

We discard galaxies that were undetected in our CO observations. Our final sample thus selected contains 79 galaxies. Among these, 38 are LINERs/Composites/Seyferts and 41 are inactive galaxies.

3.2 A link between gas-phase metallicity gradients and depletion times in AGN-like galaxies below the MS

For the optically-selected type 2 AGN, LINERs and Composites in our sample described above in Section 3.1, we find a strong relation between gas-phase metallicity gradients and molecular gas depletion time *below the MS*, which is shown in Fig 2 in the top panel. The correlation is strong with an associated p-value of ∼ 0.001 and r-value of 0.56, as annotated in the top of the figure together with the best linear fit (slope: 0.07). The Seyfert AGN are coloured in black, while the LINERs and Composites are shown in purple, and for CO non-detections, upper limits are indicated via an arrow (but not included in the analysis). The best-fit relation is overplotted as a black line while the red lines represent different MCMC-sampled fits from the `linmix` module[3], which repeatedly perturbs the datapoints within their uncertainties and reruns the fitting. The middle panel displays the $\nabla Z - t_{\rm dep}$ plane for inactive galaxies (i.e. that show no optical signs of LINER or AGN character in their central spaxels according to the BPT selection), where we find no evidence for a correlation (although the picture could conceivably change when increasing the number statistics after a future MASCOT data release). We note that it has been cautioned against using the O3N2 metallicity prescription in AGN due to its sensitivity to ionisation (Kewley et al. 2019; Fig 9), with theoretical predictions suggesting it to vary by over 2 dex e.g. at solar metallicity when evaluated over an ionisation grid going from log $U = -3.98$ to -1.98, while, as discussed in Section 3.1, e.g. Kumari et al. (2019) found the diagnostic to be very robust in LINERs and DIG regions based on studying HII–DIG/LI(N)ER pairs in nearby spirals (as well as including Seyfert-classified regions provided they fell into the outskirts of a galaxy rather than its centre). In Section 3.3, we will conduct a sanity check using a different metallicity diagnostic. For now, in the bottom panel of Fig 2, we show the relation excluding Seyfert AGN and focusing on LINERs/Composites only. The correlation coefficient $r = 0.54$ and p-value $p = 0.005$ still support a strong correlation. We also checked that the correlation is still significant with $p = 0.017$ when excluding both the Seyferts and the single datapoint with the longest depletion time. The $\nabla Z - t_{\rm dep}$ relation does thus not depend on the inclusion of type 2 Seyert AGN.

The depletion time $t_{\rm dep} = M_{\rm H_2}/{\rm SFR}$ on the x-axis is inversely related to how efficiently a galaxy is converting its remaining H_2 gas into stars. It is thus an important quantity in galaxy evolution, particularly in the below-MS regime, where one may simplistically interpret it as a measure of how quenched a system is, though the picture becomes more complicated when considering that not all systems below the MS are indeed in the process of being quenched - some may conceivably move back to the blue cloud in the future following SFR fluctuations (see e.g. Chauke et al. 2019 for rejuvenation events in LEGA-C galaxies). Within this context, Colombo et al. (2020) recently used resolved molecular gas properties and optical-IFU data from the EDGE-CALIFA survey to argue that once a galaxy is moved below the MS due to a central shortage of molecular gas, the depletion time then becomes the main driver that pushes the galaxy further towards quiescence. The relation we find in Fig 2 thus supports a picture in which any mechanism(s) that quench AGN-like galaxies also flatten or invert metallicity gradients in the process.

Given the close link between longer depletion times and declining star-forming activity below the MS (e.g. Saintonge et al.

[2] https://sdss-mangadap.readthedocs.io/en/latest/metadatamodel.html

[3] https://linmix.readthedocs.io/en/latest/

Optical AGN
+ LINERs
+ Composites

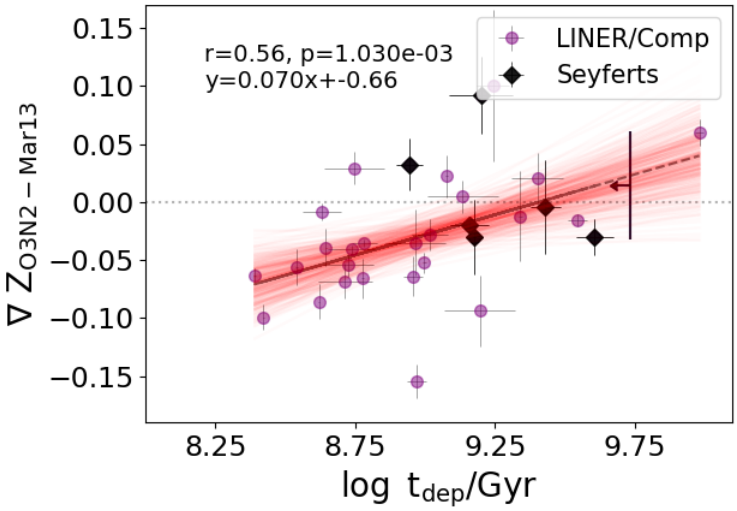

Inactive
galaxies

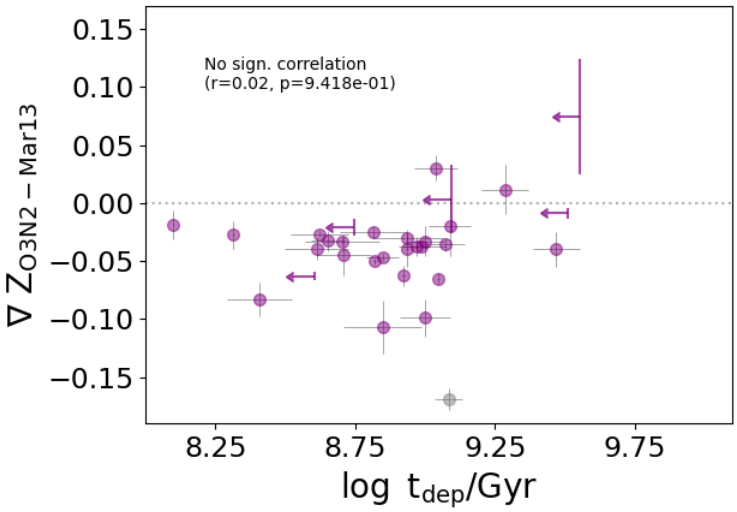

LINERs
+ Composites

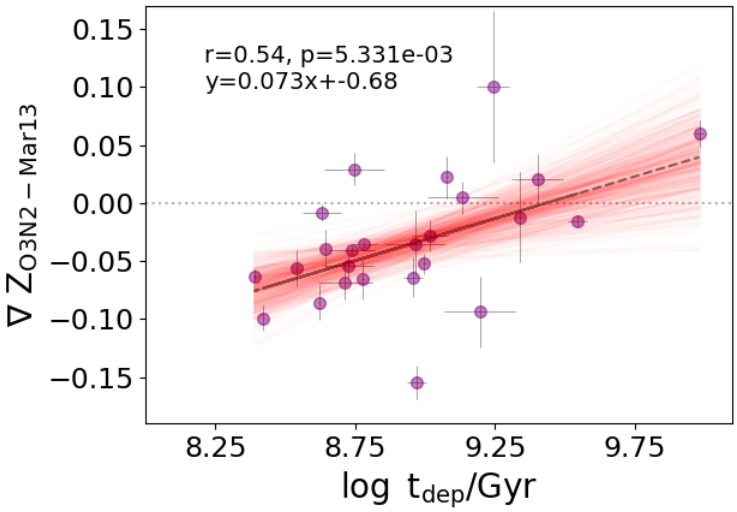

Figure 2. Metallicity gradients ∇Z as a function of depletion time $t_{\rm dep} = M_{\rm H_2}/{\rm SFR}$ below the MS. *Top panel*: Relation for AGN, LINERs and Composites. Seyfert AGN are highlighted in black, whereas LINERs and Composites are shown in purple. *Middle panel*: For the inactive galaxies in our sample, we find no correlation. *Bottom panel*: Relation for LINERs and Composites - discarding AGN due to concerns about the applicability of the O3N2 metallicity prescription, but including LINERs given the robustness of the O3N2 calibration in Kumari et al. (2019). In the top and bottom panels, the best-fit relation is overplotted as a black line, with uncertainties illustrated by the red transparent lines. Upper limits are shown by arrows and excluded from the analysis. The correlation is significant in all panels except for the inactive galaxies (see annotated p-values and r-values).

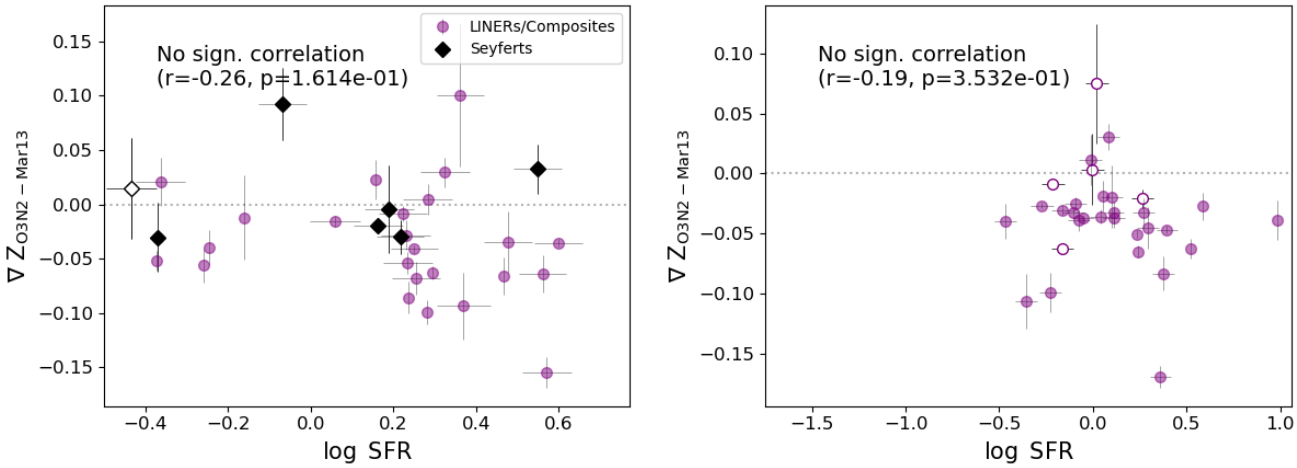

Figure 3. Metallicity gradients plotted against SFR values. In the left panel corresponding to AGN, LINERs and Composites, the optically-selected Seyfert AGN are highlighted in black, while the purple datapoints correspond to LINERs and Composites. The right panel focuses on inactive galaxies instead. In both panels, we report no correlation between ∇Z and SFR. We thus conclude that we cannot trace back the $\nabla Z - t_{\rm dep}$ relation from Fig 2 to a pure relation with SFR.

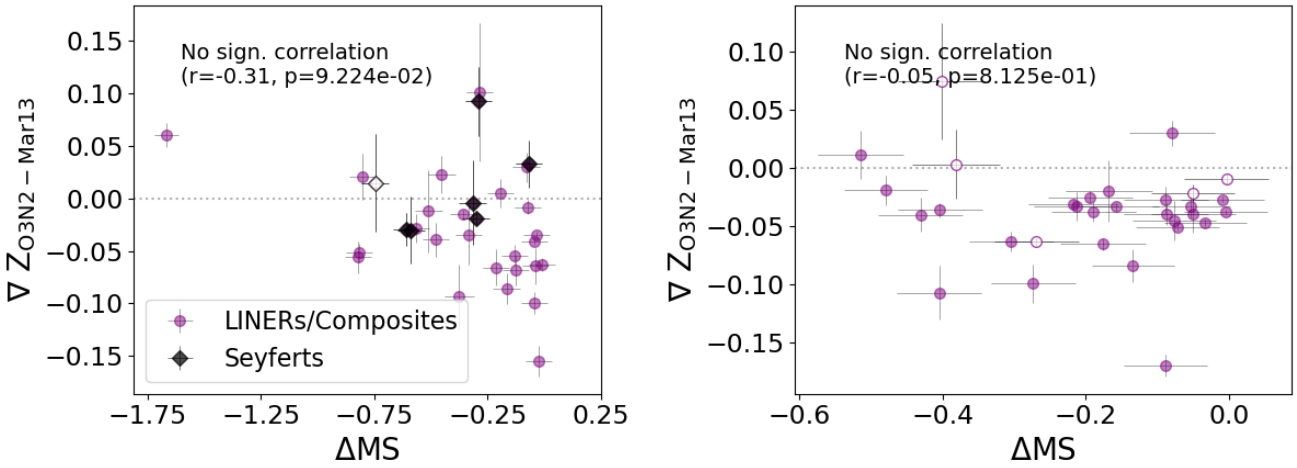

Figure 4. Metallicity gradients plotted against MS offset ΔMS = log SFR − log $\rm SFR_{RP15}$. For AGN/LINERs/Composites (*left panel*) and inactive galaxies (*right panel*) alike, there is no correlation. This indicates that variations in ∇Z are primarily driven by $t_{\rm dep}$ (relation in Fig 2) rather than MS offset.

2017, Wylezalek et al. 2022), it is instructive to contrast the metallicity gradients also against SFRs and MS offsets instead of depletion time . In Fig 3, we look for a relation between ∇Z and SFR, with AGN/LINERs/Composites shown in the left panel and inactive galaxies in the right panel. In the left panel, the black symbols denote BPT-selected Seyfert AGN, while the purple dots show LINERs and Composites. Galaxies which were CO-undetected are shown via open circles. We note that while we use the Pipe3D SSP-derived SFR values in this plot, the associated SSP-derived errors are likely to be underestimated since they merely describe how easily a best-fit SFR value can be found among all templates. We therefore choose to use Hα-derived uncertainties. Both for active and inactive galaxies alike, there is no evidence for a correlation between ∇Z and SFR. We will however revisit the impact of star formation in a resolved fashion in Section 4.2. In Figure 4, we also contrast the ∇Z values to the MS offset ΔMS = log SFR − log $\rm SFR_{RP15}$ w.r.t the Renzini & Peng (2015) prescription for the MS, again finding no correlation for active (*left panel*) and inactive (*right panel*) galaxies alike. All things considered, Figures 3 and 4 indicate that the metallicity gradients are primarily driven by the depletion time rather than SFR or MS offset. Thus, the crucial factor is not the absolute star formation, but rather the efficiency of star formation in relation to how much building material is still left in the form of cold molecular gas.

Finally, it is necessary to check for the presence of mass effects which may impact our results. In particular, we note that as can be seen in Fig 1, the AGN/LINERs/Composites in our sample fall at somewhat higher masses than the inactive galaxies on average, which could a priori complicate a direct comparison between them. For those galaxies that pass our selection criteria, we find that inactive galaxies are distributed around a median mass of log $M_\star$ = 10.45 with a spread of 0.37 dex, while the AGN/LINERs/Composites show a median mass of log $M_\star$ = 10.63 with 0.25 dex scatter. Importantly, in Figure 5, we show that there is no correlation between metallicity gradients and stellar mass either for AGN/LINERs/Composites (*left panel*) or inactive galaxies

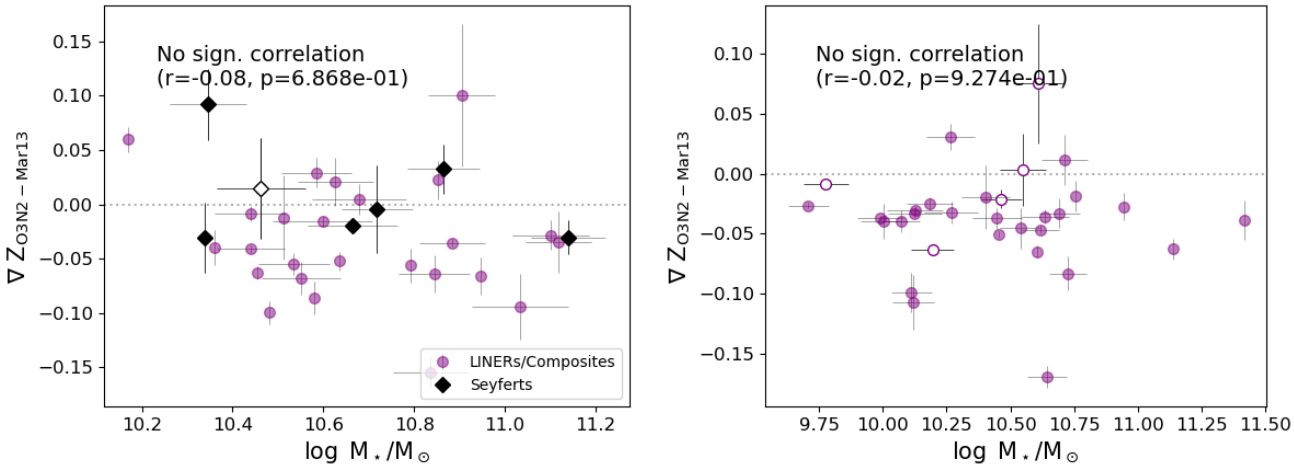

Figure 5. Metallicity gradients ∇Z plotted against stellar mass $M_\star$. We do not find any correlation in either AGN/LINERs/Composites (left panel) or inactive galaxies (right panel), so we conclude that mass effects cannot explain the $\nabla Z - t_{\rm dep}$ relation found in Fig 2.

(*right panel*). Thus, we do not suspect that mass effects play a role in the $\nabla Z - t_{\rm dep}$ relation in the AGN-like objects in our sample.

3.3 Sanity checks investigating potential unphysical drivers of the relation

Before we go into a discussion on possible physical interpretations for the ∇Z - $t_{\rm dep}$ relation presented in Section 3, we will first test the robustness of these results with respect to key aspects of our adopted methodology.

Firstly, it is important to note that in Fig 2 the x-and y-axes are likely not fully independent of each other. As described in Section 2.1, our molecular gas masses are derived from our observed CO fluxes using the $\alpha_{\rm CO}$ conversion factor from Accurso et al. (2017), which depends on galaxy-integrated metallicity (as well as offset from the star-forming Main Sequence). It is therefore necessary to check how our results may vary when using a constant $\alpha_{\rm CO}$ factor instead to derive H_2 masses and associated depletion times. In Fig 6, we use a constant value of 4.36 $M_\odot/(K\ km\ s^{-1}\ pc^{-2})$ for $\alpha_{\rm CO}$ corresponding to the canonical Milky Way value, and plot the resulting ∇Z - $t_{\rm dep}$ relation. For the AGN/LINERs/Composites (left panel) and LINERs+Composites (right panel), we still obtain a significant $\nabla Z - t_{\rm dep}$ relation with similar slopes than in Fig 2 (as well as no relation for inactive galaxies in the middle panel).

As a second check, we verify that our results do not depend entirely on our choice of metallicity prescription. For this, we explore using gas-phase metallicity gradients from the Pipe3D catalog based on the Tremonti et al. (2004) R23 calibration instead of the Marino et al. (2013) O3N2 diagnostic, since the former has been shown to be practically insensitive to the ionisation parameter U in the regime with $\log(O/H) + 12 > 8.5$ when evaluated over $-3.98 < U < -1.98$ (Kewley et al. 2019). We retrieve a metallicity range of $8.62 < \log(O/H) + 12 < 8.89$ for all galaxies passing our sample selection. We show the resulting ∇Z - $t_{\rm dep}$ relation based on the R23 calibrator in Fig 7, where the left panel again corresponds to AGN+LINERs+Composites, the middle panel to inactive galaxies, and the right panel to LINERs+Composites. In all cases except for the inactive galaxies, we recover a significant correlation. Interestingly, compared to Fig 2, we obtain a significantly steeper slope. However, we choose to proceed with the metallicity gradients obtained via the Marino et al. (2013) O3N2 method, given that many of our galaxies are affected by DIG and/or LINER emission, in which the robustness of the O3N2 calibrator has been tested as summarised in Section 3.1 (while such a test has, to our knowledge, not been conducted for R23).

4 DISCUSSION

In this Section, we will discuss various interpretations of the origin of the $\nabla Z - t_{\rm dep}$ relation presented in Section 3.2.

4.1 Outflow scenario

The metallicity gradients within galaxies are imminently responsive to gas accretion and feedback. In this Section we consider the scenario of metal-enriched outflows redistributing metals and facilitating chemical mixing within galaxies. In this picture, we hypothesise that the below-MS galaxies with longer depletion times in our Figure 2 show flatter metallicity gradients as they are (simplistically) at a later evolutionary stage such that feedback already had more time to operate than in those galaxies with short $t_{\rm dep}$ that are still more efficiently forming stars.

Observational outflow studies have traditionally had a strong focus on the most luminous AGN and starbursts; in recent years however, ionised outflows have been shown to be present in low-luminosity AGN as well as "typical" star-forming galaxies though with limited impact as assessed via coupling efficiency or mass outflow rates (Wylezalek et al. 2020; Avery et al. 2021). In particular, in the context of AGN feedback, it has been suggested that it is the integrated effect over time that makes galaxies quench given that black hole mass estimates have been found to hold the most predictive power over galaxies' quenching status (Bluck et al. 2020; Piotrowska et al. 2021). In this sense, outflows below the MS - despite being likely weak - could be the "final straw" that pushes galaxies towards quiescence after having been subjected to gas removal/heating on long timescales via continuous energy injection. In the context of stellar feedback, from a simulations perspective, Gibson et al. (2013) find that even weak SN feedback leads to efficient gas mixing on cosmological timescales as manifested by a flattening of metallicity gradients towards low redshifts in the MUGS

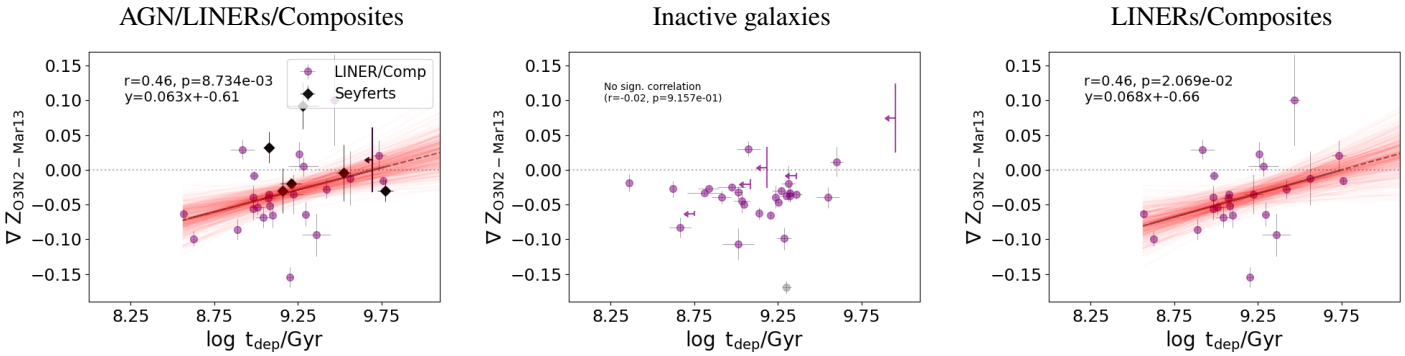

Figure 6. Same as Fig 2, but recalculating the depletion time with a constant CO-to-H_2 conversion factor $\alpha_{CO} = 4.36$ $M_\odot/(K\ km\ s^{-1}\ pc^{-2})$ corresponding to the canonical Milky Way value.

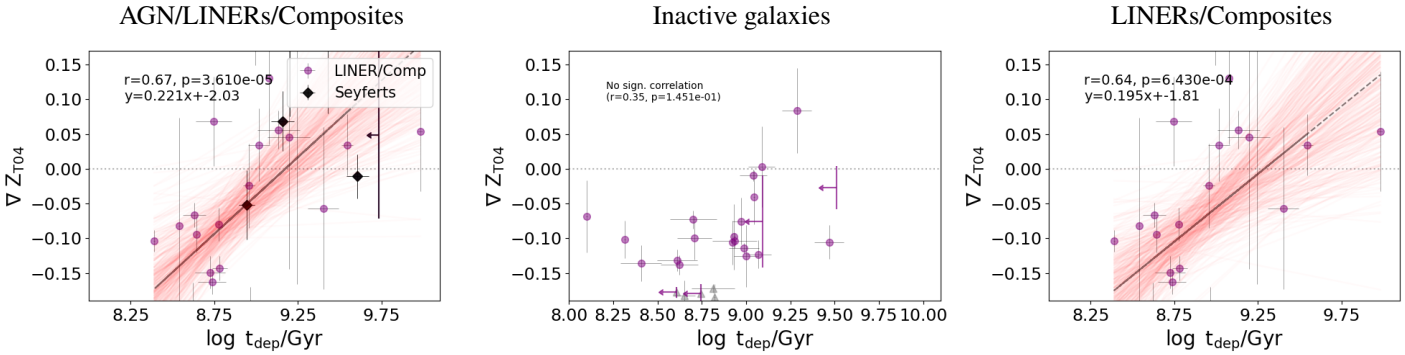

Figure 7. Same as Fig 2, but using the Pipe3D gas-phase metallicity gradients based on the Tremonti et al. (2004) R23 calibrator instead of the Marino et al. (2013) O3N2 prescription.

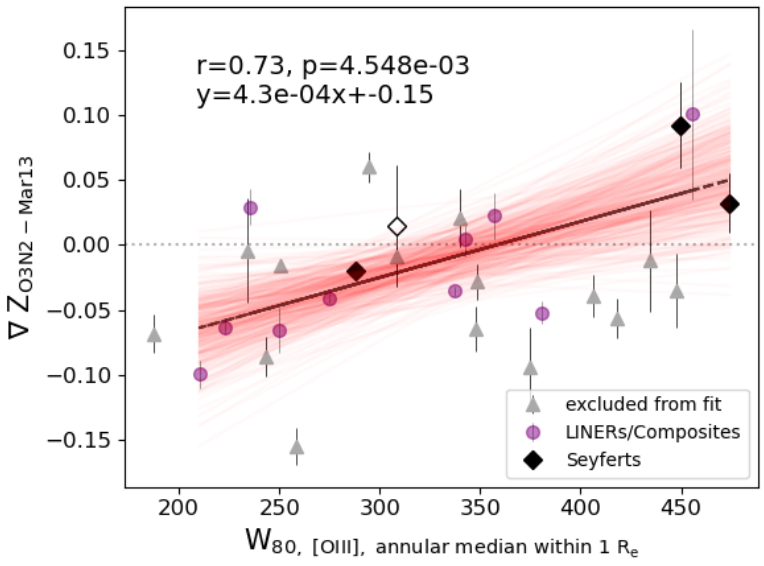

Figure 8. Gas-phase metallicity gradients ∇Z plotted against the annular median [O III] W_{80} parameter within 1 R_e. For each galaxy, we first recovered a W_{80} profile in annuli spanning 0.1 R_e in width, and then calculated the median W_{80} across its annuli within 1 R_e. We find a strong correlation between ∇Z and annular median [O III] W_{80} in Seyfert AGN (black datapoints) and LINERs/Composites (purple dots). We suggest that this relation emerges via weak chemically-enriched outflows. The targets plotted in grey are excluded from the fit due to exhibiting too many spaxels in which we deem the recovered W_{80} values to be unreliable ($S/N < 10$, 'DONOTUSE' flag, or negative flux). Only targets with > 10 % of reliable spaxels are included in the fit. The best linear fit is shown as a black solid line, while the red lines show fits recovered when perturbing the datapoints within their uncertainties. The r-value, p-value and coefficients of the best fit are further annotated in the top of the panel.

suite (Stinson et al. 2010), while stronger feedback produced flat metallicity gradients throughout cosmic time. The adiabatic blast-wave model feedback used in these results operates via thermal energy injection into the gas surrounding stellar particles (with the "strong" model given twice the heating power of the "weak" model, plus radiation feedback). It therefore does not necessarily manifest in terms of strong outflows and may thus be challenging to constrain observationally, but we will nevertheless explore a quick kinematic analysis to see if any outflow signatures can be found. The importance of AGN feedback has also been highlighted in Illustris TNG50 simulations, where Hemler et al. (2021) argue that it may likely contribute significantly to the shallow metallicity gradients recovered at low redshift (next to stellar feedback), especially in high-mass galaxies where kinetic mode AGN feedback kicks in.

Going back to observations, metal-enriched outflows on galactic scales have been shown to be ubiquitous in high-redshift massive star-forming galaxies (see e.g. the review by Veilleux et al. 2005). At low redshift, there have also been observational hints that feedback mechanisms may play a strong role in shaping the metallicity distribution within galaxies. For instance, Baker et al. (2022) investigate the predictors of resolved metallicities in star-forming MaNGA galaxies, and find intringuingly that there is a stronger anti-correlation with global SFR than with the local one (though both local and global quantities matter), which is broadly consistent with large-scale stellar feedback-driven winds ejecting or redistributing metals. Avery et al. (2021) further find evidence for an enhanced dust attenuation within the outflows of MaNGA galaxies, which could potentially be traced back to metal enrichment, while Chisholm et al. (2018) confirmed the high level of metal enrichment in the outflows of seven local star-forming galaxies using HST/COS spectra.

In light of these considerations, as a first step, we are searching for kinematics signatures of ouflows in the [O III] line tracing ionised gas. First, we calculate line width profiles by taking the [O III] maps from the MaNGA DAP and imposing a signal-to-noise threshold S/N > 3, while discarding spaxels with a "DONOTUSE" flag, as well as negative fluxes. We further discard galaxies in which less than 10 % of spaxels fulfill the aforementioned criteria. In each selected spaxel, we then calculate W_{80}, defined as the spectral width that encompasses 80 percent of the total line flux. For this purpose, the line profiles are fit with a single or double Gaussian, where a second component is only permitted if it has a signal-to-noise S/N > 3 to prevent noise fitting. Skylines are masked. Within annuli of $0.1R_e$, we then extract the median W_{80} value at the corresponding radius, where each spaxel is weighted by the fraction of its area that falls into the annulus. The methodology will be described in more detail in an upcoming paper investigating kinematic signatures in different types of AGN (Alban et al. 2022).

In Figure 8, we first attempt to identify indications of kinematic AGN feedback in the more central regions by contrasting the metallicity gradients to the median [O III] W_{80} within $1R_e$ for our sample of AGN-like galaxies. Grey dots show the location of galaxies that were discarded due to less than 10 % of their spaxels fulfilling our selection criteria outlined above, and are excluded from the correlation analysis. In the left panel, black datapoints denote Seyfert AGN, while LINERs/Composites are shown in purple. We note that our approach is complicated by the fact that not all of our AGN-like objects are indeed Seyfert AGN. It remains debated whether LINER emission can primarily be traced back to central AGN activity (Márquez et al. 2017), ionisation via post-AGB stars (Singh et al. 2013), or other ionisation sources. Nevertheless, there is a significant correlation of central [O III] line width with $r = 0.73$,

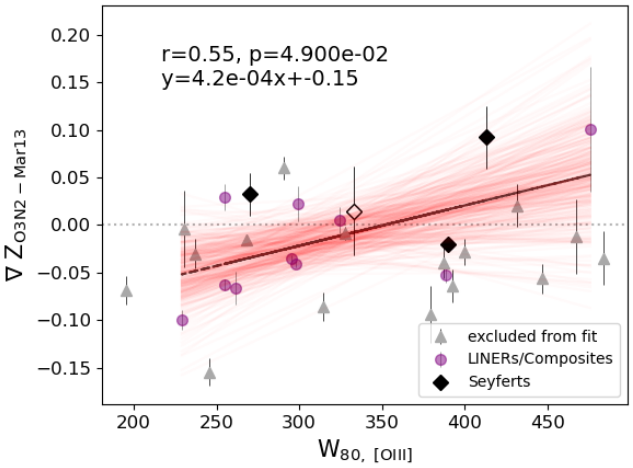

Figure 9. Metallicity gradients plotted against galaxy-integrated W_{80} measurements from the [O III] line, showing a tentative correlation. The purple dots correspond to LINERs/Composites, while the black datapoints are Seyfert AGN. The targets plotted in grey are excluded from the fit due to exhibiting too many spaxels in which we deem the recovered W_{80} values to be unreliable ($S/N < 10$, 'DONOTUSE' flag, or negative flux). Only targets with > 10 % of reliable spaxels are included in the fit. The best linear fit is shown as a black solid line, while the red lines show fits recovered when perturbing the datapoints within their uncertainties. The r-value, p-value and coefficients of the best fit are further annotated in the top of the panel.

$p < 0.005$, which we interpret as a strong indicator of a causal link between outflow kinematics and the chemical distribution in AGN-like objects. We argue again that the trend cannot be explained by mass effects, given that we found no relation between ∇Z and stellar mass in Fig 5 (Section 3.3). We further checked that the same trend is not seen in inactive galaxies. We highlight that the W_{80} values fall below $< 500\ \mathrm{km\ s^{-1}}$ and would thus not be regarded as outflow signatures in studies on the Main Sequence. However, below the Main Sequence we expect signatures to weaken, and as outlined above, weak feedback may still play a significant role in this regime. We thus favour an interpretation in which weak outflows may not be formally detected when using line widths as a tracer, but still exist.

To explore a possible impact of feedback (AGN or stellar) on global scales, we further contrast the metallicity gradients against the galaxy-integrated [O III] W_{80} in Fig 9 for our AGN/LINERs/Composites. In this case, we still find a tentative $\nabla(Z) - W_{80}$ relation ($p = 0.049$), which may potentially be attributed to galactic-scale gas flows redistributing the enriched medium, though we caution that the correlation is only marginally significant. Again, we checked that such a relation is not present for the inactive galaxies in our sample.

We then proceed to study the cold gas kinematics of the AGN-like objects in Fig 10. In the left panel, we plot the metallicity gradients as a function of the W_{90} value obtained from our galaxy-integrated velocity profiles, i.e. the width containing 90 % of the CO line flux. The CO line is fitted by a single or double Gaussian as required, as outlined in Wylezalek et al. (2022). We do not find any significant relation, although we note an "empty triangle" region such that no objects fall into the regime with large W_{90} and substantially negative ∇Z. Similarly, we find no relation in the right panel of Fig 10 when contrasting the metallicity gradients to the velocity offset between our observed CO line peak and the rest-frame wavelength. We also checked that there is no relation between global

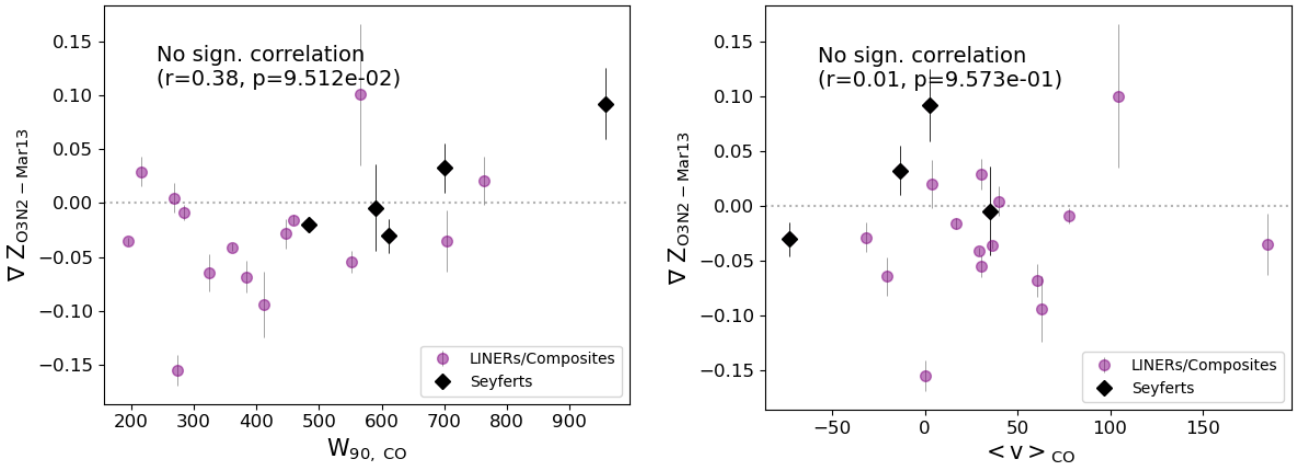

Figure 10. *Left panel*: Metallicity gradients plotted against the W_{90} measurement from the galaxy-integrated CO profiles of our AGN, LINERs and Composites. *Right panel*: Metallicity gradients plotted against the median velocity offset in our galaxy-integrated CO profiles.

cold gas kinematics and metallicity gradients in the inactive galaxies. We note that our single-dish observations do not allow us to explore resolved kinematics of the neutral gas phase, and molecular outflow signatures are more challenging to detect on a global scale.

To conclude this section, considering the [O III] ionised gas kinematics in AGN-like galaxies in Fig 8 we suggest that weak outflows below the Main Sequence could plausibly drive chemical mixing in AGN/LINERs/Composites while prolongating depletion times (i.e. reducing star-forming efficiency) and possibly driving those galaxies towards quiescence in a "last straw" scenario. Our findings raise the question of how metal-mixing timescales compare to AGN lifetimes. AGN have been suggested to "flicker" on and off in many consecutive short cycles of $\sim 10^5$ yr amounting to a total lifetime of 10 Myr−1Gyr as estimated from e.g. the Soltan argument (Schawinski et al. 2015). However, it is not clear a priori how the outflow strength in AGN varies across their lifetime. Our naïve assumption is that the galaxies with stronger outflow signatures in Fig 8 (and flatter/positive metallicity gradients) are "older" to allow more time for metal redistribution, though the exact time required for that is also challenging to constrain. For instance, using a toy model describing metal production based on the observed SFR density profiles of $z \sim 1$ galaxies, Simons et al. (2021) argue that in the absence of any redistribution mechanism, galaxies would develop rapidly declining metallicity gradients incompatible with observations on timescales of $\sim 10 - 100$ Myr, which may thus be regarded as an upper limit to metal mixing timescales.

4.2 Connection to fluctuations in local star-forming activity

It is well established that the global metallicities of galaxies are linked to both global stellar mass and SFR (the "fundamental metallicity relation"; Ellison et al. 2008, Mannucci et al. 2010). It has further been proposed that this global relation may (partially) arise from local scalings between the resolved stellar mass, SFR and oxygen abundance. For instance, Barrera-Ballesteros et al. (2016) confirm the existence of a local mass-metallicity relation, while they find no evidence for a secondary relation with SFR surface density $\Sigma_{\rm SFR}$. On the other hand, Sánchez Almeida & Sánchez-Menguiano (2019) and Baker et al. (2022) report a local anti-correlation between $\Sigma_{\rm SFR}$ and metallicity at fixed mass in MaNGA galaxies (see also the review by Maiolino & Mannucci 2019). This has been attributed to localised inflows fuelling star formation whilst diluting the enriched gas, though Baker et al. (2022) highlight the even stronger importance of the global SFR in setting local metallicities. The significance of the global SFR could possibly be attributed to the transport of metals by galactic-scale winds driven by stellar feedback.

In this section, we contemplate the possibility that the $\nabla Z - t_{\rm dep}$ relation may arise due to variations in local in-situ star formation which simultaneously link to the resolved metallicities and affect the local depletion time $t_{\rm dep} = M_{\rm H_2}/{\rm SFR}$. To evaluate variations in SFR whilst controlling for stellar mass, we derive the radially resolved $\Sigma_{\rm SFR}$-$\Sigma_\star$ distribution for our below-MS sample as follows: We subdivide each galaxy in our sample into annuli of 0.2 R_e width, and run our full spectral fitting procedure (described in section 2.3.3 along with a comparison between our recovered global SFR & $M_\star$ and the Pipe3D reference values) on the annular spectra. We thus recover the SFR surface density and stellar mass surface density in individual annuli, which we show as a scatter plot in the left panel of Fig 11 for our AGN-like objects, with the median baseline shown as a black solid line.

We then proceed to calculate, for each AGN/LINER/Composite, the radial profile of the offset $\Delta\Sigma_{\rm SFR}$ between $\Sigma_{\rm SFR}$ and the median value at fixed mass ($\langle\Sigma_{\rm SFR}(\Sigma_\star)\rangle$) in our sample, and analyse how they vary as a function of depletion time. In the right panel of Fig 11, we classify the resulting profiles in two bins according to their depletion time, as indicated by the colour (blue/red = short/long $t_{\rm dep}$). The dashed lines indicate the median profile in each $t_{\rm dep}$ bin, and the shaded regions indicate the spread between profiles. We find a trend with $t_{\rm dep}$ when controlling for mass: objects with longer depletion time (and thus flatter/positive metallicity gradients according to our $\nabla Z - t_{\rm dep}$ relation) show a suppression of star formation in their outskirts compared to objects with short $t_{\rm dep}$ whilst exhibiting similar levels of star formation in the centre. Within the context of the resolved fundamental metallicity relation, the drop in SFR in the outskirts may drive higher local metallicities at large radii, thus flattening or inverting gradients compared to AGN/LINERs/Composites with short $t_{\rm dep}$. It is interesting to note that despite our results on outflows in the previous Section 4.1, the more quenched galaxies

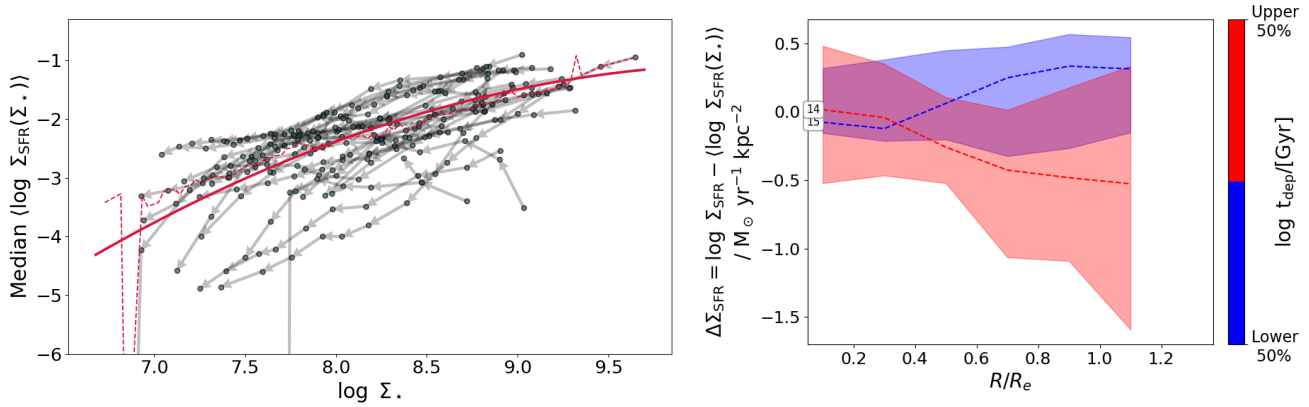

Figure 11. *Left panel*: The individual dots show the $\Sigma_{\rm SFR}$-$\Sigma_\star$ distribution of our AGN/LINERs/Composites sample using annuli of 0.2 R_e width, with the red solid line showing the median SFR surface density $\langle\Sigma_{\rm SFR}(\Sigma_\star)\rangle$ for a given mass. Each grey background curve corresponds to a single galaxy, with each data point on the curve corresponding to an individual annulus, such that the arrows show the path taken in the $\Sigma_{\rm SFR} - \Sigma_\star$ plane when going from the centre-most annulus to the outermost one. *Right panel*: Radial profiles of the offset $\Delta\Sigma_{\rm SFR}$ from the median of the $\Sigma_{\rm SFR}$-$\Sigma_\star$ distribution spanned by our sample (solid line in top panels), i.e. offset between SFR surface density $\Sigma_{\rm SFR}$ within a given annulus and the median SFR surface density $\langle\Sigma_{\rm SFR}(\Sigma_\star)\rangle$ evaluated at the stellar mass contained within the annulus. In each panel, the sample is sub-divided into galaxies with longer/shorter depletion times (upper/lower 50th percentile of $t_{\rm dep}$), as indicated by red/blue colouring. The dashed lines show the median profile in a given $t_{\rm dep}$ bin, with associated spread illustrated by the shaded regions. The AGN-like objects with long depletion times show a similar central star-forming activity at fixed mass than those with short depletion times, but are comparatively more passive in the outskirts.

with long depletion times are suppressed in star formation primarily in the outskirts. The weak character of the outflows may indicate that while they can mix gas efficiently within galaxies, they do not permanently remove it from their centre. In fact, the deficit of star formation in the outskirts is more broadly in line with e.g. radiative feedback scenario heating up the surrounding medium to prevent new inflows. For inactive galaxies (omitted from Fig 11), we could not easily identify any trend with $t_{\rm dep}$ in the shape of Δ ΣSFR profiles which exhibited large spreads.

Given these results, the metallicity gradients of our sample of AGN-like objects may indeed be partially explained by a connection to in-situ star formation, though our results on the importance of outflows in the previous Section 4.1 suggest that this is not the whole picture. We conclude for now that in AGN-like objects, the observed $\nabla Z - t_{\rm dep}$ relation may arise as a combination of at least two drivers. We proceed to consider other factors (inflows, mergers and morphological factors) in the following sections.

4.3 Inflow scenario

In this Section we consider the possibility of radial inflows of pristine/metal-poor gas funneled directly to the central regions of galaxies causing flatter/positive metallicity gradients by diluting the central regions in those galaxies that have long depletion times. For nearby galaxies on the MS, it has been found that local metallicities are correlated with the galaxy-integrated *atomic* gas fraction (Lutz et al. 2021). We note that the inflow scenario may not be as straight-forward for the galaxies in our sample, given that these all fall below the Main Sequence by selection and one may therefore in general expect them to be more gas-deficient (e.g. Saintonge et al. 2017). Nevertheless, it is not impossible for galaxies below the MS to contain a significant amount of gas without star formation being fuelled (though this appears to be more often the case for atomic hydrogen, see e.g. Janowiecki et al. 2020). For instance the gas may be stabilised against fragmentation and collapse via morphological transformation (Martig et al. 2009). In Section 4.5, we will discuss potential impacts of morphology in more detail. Here we explore instead how the metallicity gradients behave as a function of CO luminosity, H_2 mass and H_2 fraction for our sample to check if there is any direct evidence of recent gas inflows manifesting via an enhanced amount of gas.

In Figure 12, we contrast ∇Z to the molecular gas mass $M_{\rm H_2}$ in the left panel, to the CO luminosity $L_{\rm CO}$ in the middle panel and the molecular gas fraction $f_{\rm H_2} = M_{\rm H_2}/M_\star$ in the right panel. In either case, we do not find any evidence for a correlation. For inactive galaxies omitted from Fig 12, we similarly do not find any evidence for inflows driving the observed metallicity gradients. We note however that localised inflows that do not propagate to galaxy-wide scales would be challenging to detect given our unresolved CO observations. Within this context, interestingly, a recent statistical study of the resolved fundamental metallicity relation in MaNGA galaxies (Baker et al. 2022) found that the strongest predictors of local metallicity were not the local SFR surface density (and local stellar mass surface density), but instead the global SFR and global stellar mass. The fact that the local SFR is only of secondary importance in setting local metallicities argues also against localised inflows being a primary driver (as inferred via the resolved KS relation; Kennicutt 1998; Schmidt 1959).

4.4 Merger scenario

Aside from in-situ chemical evolution and metal transport due to inflows or feedback processes, the metallicity distribution within galaxies may be affected by merging events during their lifetime. Galaxy interactions are thought to flatten metallicity gradients as a consequence of chemical mixing as well as metal-poor gas inflows reaching the centre. This behaviour has indeed been observed e.g. in LIRGs at various merger stages (Rich et al. 2012), as well as optically- and IR-selected early-stage spiral–spiral interactions (Rupke et al. 2010). On the other hand, in a sample of 36 post-merger MaNGA galaxies, the local metallicity has been found to be

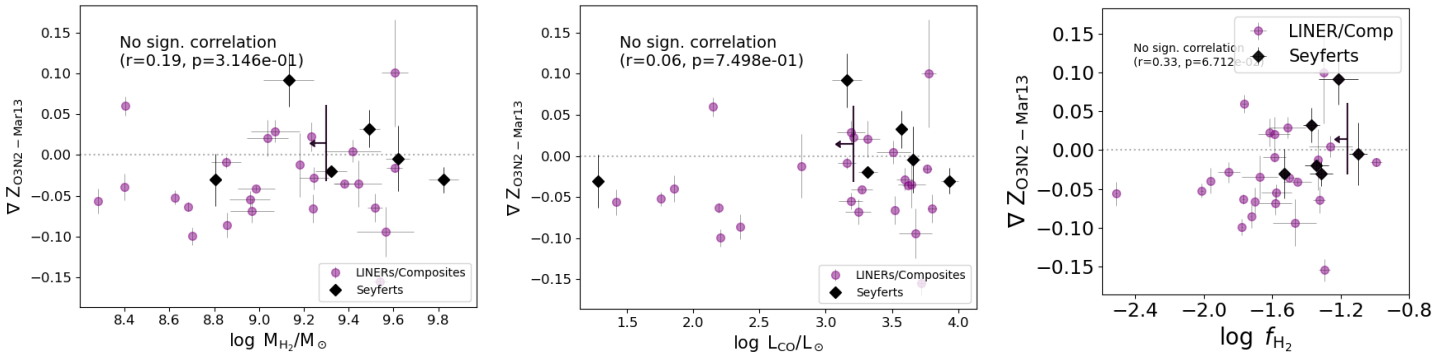

Figure 12. Metallicity gradients plotted against molecular gas mass (top row) and CO luminosity (bottom row). The left panels correspond to AGN/LINERs/Composites, while the right panels focus on inactive galaxies. We do not see any correlation in any of these panels.

suppressed in the outskirts while not being significantly affected in the central regions (Thorp et al. 2019).

While we have already attempted to exclude ongoing mergers from our analysis by identifying them visually from the SDSS multi-band images as noted in Section 3, it is still possible for our sample to include post-merger galaxies which are no longer identifiable via morphological traits. Therefore, while a full kinematic axis analysis is beyond the scope of this work, we perform a simple visual inspection of the stellar and gas-phase velocity maps of our sample to identify galaxies that show potential signs of a misalignement between their stellar and gas-phase dynamics. We point out that even this simple exercise can become challenging in the below-MS regime due to the weakness of the lines required to derive velocity maps. In Appendix A, we show the maps of gas-phase velocity as traced by Hα and [O III] λ5007 as well as stellar velocity for our sample of optically-identified LINERs, Composites and Seyferts (Fig A3). These plots have been generated using the MaNGA DAP and the MARVIN package (Cherinka et al. 2019) with Voronoi binning and a minimum S/N of 3 for a given spaxel. In general, we conclude that for the majority of our sample, the kinematics of the stellar and gas-phase components are consistent with rotating in an aligned manner. However, we flag a number of objects that show *potential* signs of misalignement. In detail, we verified that our results are not strongly affected when removing the AGN-like galaxies with the following IDs: 8588-6101, 8595-3703, 8084-6103. Updated versions of Figs 2 and 8 excluding the targets listed above are presented in the appendix (Fig A1).

Finally, it is still an open question for how long the optical and kinematic signature of mergers remain detectable. For instance, using `GADGET-3/SUNRISE` major merger simulations to construct mock velocity and velocity dispersion fields at the resolution of MaNGA, Nevin et al. (2021) broadly retrieve kinematic observability timescales of 0.9 − 6 Gyr. On the other hand, Lotz et al. (2008) find that post-merger galaxies may become undetectable after just 200 Myr depending on merger parameters. We cannot exclude that long-term effects from past mergers affect our sample, but one may argue that any such effects on the gas-phase metallicities would be "washed out" again by the other factors of influence that impact the chemical reservoir more imminently: in-situ chemical evolution, inflows, and outflows. As mentioned in Section 4.1, while studies constraining the timescale for metal redistribution are yet sparse, Simons et al. (2021) argue that it should be limited to $\lesssim$ 100 Myr, as otherwise galaxies may rapidly develop metallicity gradients more negative than observed (as predicted by modelling metal production based on observed SFR surface density profiles in $z \sim 1$ 3D-HST galaxies).

4.5 Morphological scenario

As mentioned already in Section 4.3, morphological effects may influence the gas properties and metal distribution within galaxies. For example, in a morphological quenching scenario (Martig et al. 2009), the gas disk would be stabilised against fragmentation and galaxies could thus retain a significant central gas reservoir diluting local metallicities e.g. from a recent inflow even at low star-forming activity. Lutz et al. (2021) recently found evidence that the metallicity gradients in actively star-forming galaxies are primarily set by variations in stellar mass surface density. We first use the stellar mass surface density within 1 R_e ($\mu_\star = 0.5 \cdot M_\star/(\pi {R_e}^2)$) as a morphological tracer to assess broadly how morphological factors may contribute to our observed $\nabla Z - t_{\rm dep}$ relation. In the left panel of Fig 13, we contrast the metallicity gradients to $\mu_\star$ for AGN, LINERs and Composites, finding no correlation.

We then move to exploring the resolved profiles of stellar mass surface density as a function of depletion time, using the results from our full spectral fitting procedure described in Section 2.3.3. In the right panel of Fig 13, we show our recovered profiles of stellar mass surface density $\Sigma_\star = M_{\star,\rm ann}/A_{\rm ann}$, denoting the mass of stars per surface area $A_{\rm ann}$ within a given annulus of width 0.2 R_e. The top panels show the absolute $\Sigma_\star$ profiles for our AGN-like objects (left panel) and inactive galaxies (right panel), where the colour-coding reflects a binning according to depletion time $t_{\rm dep}$ (red/blue = objects that have longer/shorter depletion times than the median of the distribution). The dotted lines denote the median profiles, and the spread is indicated by the shaded regions. Clearly the two curves correponding to different $t_{\rm dep}$ bins are fully consistent with each other, such that we do not find any evidence for the stellar mass gradients being linked to depletion times.

Finally, we also report that when using the Pipe3D v/σ ratio of velocity over velocity dispersion within 1.5 R_e as a morphological indicator, we find no trend with metallicity gradients, contrary to recent results at higher redshift (out to $z = 2.5$) by Sharda et al. (2021). Further, we find no relation with the central velocity dispersion within 2.5 arcsec of either the stellar kinematics $\sigma_\star$ (when excluding the single datapoint with lowest $\sigma_\star$) or the gas dynamics as traced by Hα. We thus conclude that, at least by using the simple morphological tracers in this Section, we do not find any evidence for the metallicity gradients in our sample being influenced by morphological effects.

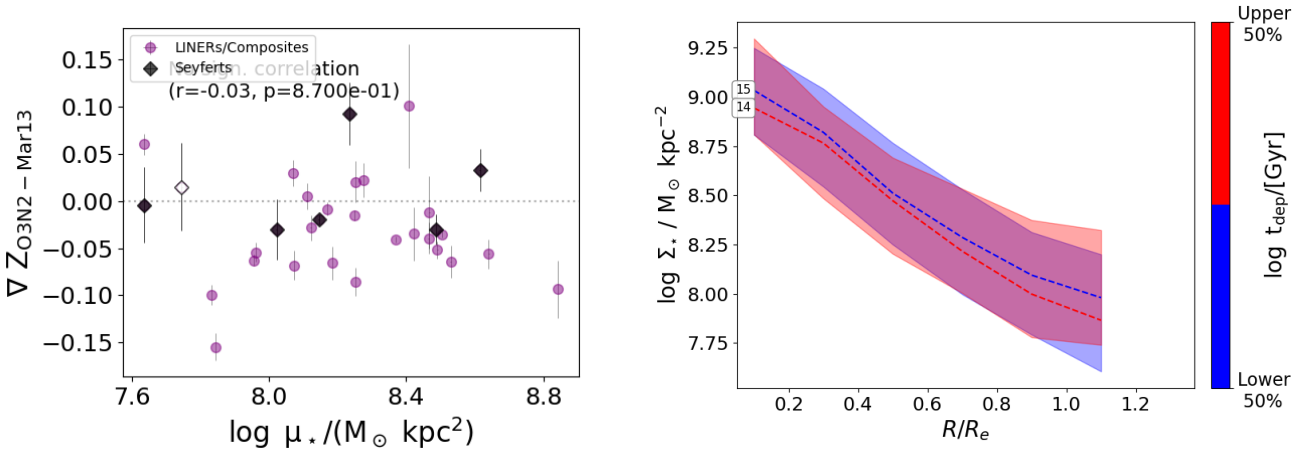

Figure 13. *Left panel*: Metallicity gradients plotted against global stellar mass surface density $\mu_\star = 0.5 \cdot M_\star/(\pi {R_e}^2)$ as a tracer of morphology for AGN, LINERs and Composites. We find no correlation. *Right panel*: Median profiles of stellar mass surface density $\Sigma_\star$ as a function of galacto-centric radius in units of the half-light radius R_e. The colour-coding refers to bins of depletion time where objects were divided into an upper and lower 50th percentile of $t_{\rm dep}$ values (i.e. red = long $t_{\rm dep}$, blue = short $t_{\rm dep}$). The median profiles in each $t_{\rm dep}$ bin are shown as dotted lines with associated spread illustrated by the shaded regions. Again, we find no link between depletion times and stellar mass surface density profiles.

5 CONCLUSIONS

In this paper, we presented a selection of early results from the MASCOT survey (Wylezalek et al. 2022), focusing on an empirically found relation between gas-phase metallicity gradients ∇Z and molecular gas depletion times $t_{\rm dep}$ in LINERs, Seyfert AGN and Composites below the Main Sequence (MS). We used oxygen abundance gradients derived via the Marino et al. (2013) O3N2 calibrator, and specifically decided to explore the below-MS regime affected by DIG emission given recent results by e.g.Kumari et al. (2019) supporting the robustness of the O3N2 metallicity calibrator in DIG/LI(N)ER-dominated regions (as discussed in more detail in Section 3.1). We excluded edge-ons, type 1 AGN, and visually identified major mergers from the analysis. Our primary results can be summarised as follows:

- The $\nabla Z - t_{\rm dep}$ relation we report is strongly significant for our sample of "AGN-like objects" combining AGN, LINERs and Composites ($p \sim 0.001, r = 0.56$). When excluding AGN (e.g. due to concerns about the accuracy of the metallicity gradients), the relation still holds for LINERs+Composites with $p \sim 0.005, r = 0.54$ (Fig 2), while no relation is found in inactive galaxies.
The relation is intriguing given that variations in depletion time (or inversely, star forming efficiency) have been suggested to be the driving factor that pushes galaxies into the passive branch once they experienced an initial central lack of molecular gas (Colombo et al. 2020). In that sense, the discovery of a $\nabla Z - t_{\rm dep}$ relation *below the MS* may suggest that whichever mechanism drives quenching in AGN-like objects also flattens or inverts metallicity gradients in the process.

- The relation cannot be traced back to a link between ∇Z and MS offset (Fig 4), nor a trend with global SFR. Further, we cannot explain the relation via the presence of mass effects, as we report no trend between ∇Z and stellar mass (Fig 5).

- We also checked that the relation persists when using a constant CO-to-H_2 conversion factor instead of a metallicity-dependent one (Fig 6), and when using metallicity gradients based on the Tremonti et al. (2004) R23 calibrator instead of the Marino et al. (2013) O3N2 prescription.

We then explored different possible physical drivers of the $\nabla Z - t_{\rm dep}$ relation in AGN/LINERs/Composites in Section 4:

- We first contemplated the scenario of metal redistribution via chemically enriched outflows. In this picture ∇Z gradients are flatter in galaxies with long depletion times, because these galaxies are simplistically at a later evolutionary stage where feedback already had more time to operate. In AGN/LINERs/Composites, we indeed found a strong link between ∇Z and e.g. the median width ("W_{80}") of the ionised [O III] λ5007 line within 1 R_e (Fig 8). We interpret this trend as a strong indication of feedback-induced chemical mixing taking place as galaxies transition to the red cloud. A tentative correlation between ∇Z and global [O III] λ5007 line width is also showing.
Interestingly, the observed velocity broadening is very modest < 500 km/s, and would thus not normally be flagged as an outflow signature. However, in a picture where galaxies quench due to the integrated effect of feedback over prolonged time (Piotrowska et al. 2021), weak feedback may represent the "final straw" that permanently decreases their star-forming efficiency. For a detailed discussion, including results from simulations, we refer the reader to Section 4.1. We find no further evidence in the global CO kinematics, likely due to the lack of spatial resolution.

- We then analysed the impact of local star formation (at fixed stellar mass). Potentially, metallicity gradients may be traced back to local variations in star-formation due to a resolved fundamental metallicity relation, which in turn may impact the global depletion time $t_{\rm dep} = M_{\rm H_2}/{\rm SFR}$. Indeed our sample of AGN/LINERs/Composites shows a connection between longer depletion times and a relative suppression of SFR surface density in the outskirts (Fig 11), unlike inactive galaxies. Next to the impact of feedback, in-situ star formation may thus contribute to shaping the $\nabla Z - t_{\rm dep}$ relation in our AGN-like objects.

- Similarly to outflows, inflows may influence metallicity gradients (though our galaxies reside below the MS). However, we find no trend when contrasting metallicity gradients to H_2 mass, CO luminosity, or molecular gas fraction $f_{H_2} = M_{H_2}/M_\star$ (Fig 12), and thus not a direct indication of gas accretion affecting the metallicity distribution. However, we note that our unresolved single-dish CO observations do not allow us to exclude the possibility of localised inflows influencing our results.

- We further considered morphological effects. For instance, galaxies could decrease in star-forming efficiency whilst preserving a gas reservoir that is dynamically stabilised against fragmentation (Martig et al. 2009). However, we find no evidence for metallicity gradients depending on stellar mass surface density within 1 R_e (Fig 13), and no difference between the stellar mass surface density profiles of high-t_{dep} and low-t_{dep} AGN-like objects. Using different morphological tracers - the v/σ ratio of velocity over velocity dispersion within 1.5 R_e, or central velocity dispersion within 2.5 arcsec (stellar or Hα) - offered no further clues.

- Given that merger activity would naturally impact the metallicity distribution within galaxies, we briefly search for merger signatures within our sample by visually comparing the Hα and [O III] gas-phase velocity maps to the stellar velocity maps. We confirmed that our results were not strongly affected when conservatively discarding any galaxies which showed *potential* signs of misalignement in stellar and gas-phase kinematics.

In conclusion, we propose that in our AGN-like targets, the observed $\nabla Z - t_{dep}$ relation arises partially as a consequence of chemical mixing due to centrally-driven outflows that increase in impact as time goes on and depletion times become longer, and is partially connected to fluctuations in local star formation, possibly via a resolved fundamental metallicity relation.

We finally note that, given the sample size of our below-MS objects, we have not considered the impact of environment on metallicity in this work (f.ex. enriched accretion onto satellites, see Schaefer et al. 2019). We defer an investigation of environmental effects on the molecular gas properties and other galaxy parameters using our full sample (below- and above-MS) to a later paper.

6 ACKNOWLEDGEMENTS

The entire MASCOT team would like to warmly thank the staff at the Arizona Radio Observatory, in particular the operators of the 12m Telescope, Clayton, Kevin, Mike and Robert, for their continued support and help with the observations.

DW is supported by through the Emmy Noether Programme of the German Research Foundation.

This research made use of Marvin, a core Python package and web framework for MaNGA data, developed by Brian Cherinka, José Sánchez-Gallego, Brett Andrews, and Joel Brownstein (Cherinka et al. 2019)[4].

This project makes use of the MaNGA-Pipe3D dataproducts. We thank the IA-UNAM MaNGA team for creating this catalogue, and the ConaCyt-180125 project for supporting them.

Funding for the Sloan Digital Sky Survey IV has been provided by the Alfred P. Sloan Foundation, the U.S. Department of Energy Office of Science, and the Participating Institutions. SDSS-IV acknowledges support and resources from the Center for High Performance Computing at the University of Utah. The SDSS website is www.sdss.org. SDSS-IV is managed by the Astrophysical Research Consortium for the Participating Institutions of the SDSS Collaboration including the Brazilian Participation Group, the Carnegie Institution for Science, Carnegie Mellon University, Center for Astrophysics | Harvard & Smithsonian, the Chilean Participation Group, the French Participation Group, Instituto de Astrofísica de Canarias, The Johns Hopkins University, Kavli Institute for the Physics and Mathematics of the Universe (IPMU) / University of Tokyo, the Korean Participation Group, Lawrence Berkeley National Laboratory, Leibniz Institut für Astrophysik Potsdam (AIP), Max-Planck-Institut für Astronomie (MPIA Heidelberg), Max-Planck-Institut für Astrophysik (MPA Garching), Max-Planck-Institut für Extraterrestrische Physik (MPE), National Astronomical Observatories of China, New Mexico State University, New York University, University of Notre Dame, Observatário Nacional / MCTI, The Ohio State University, Pennsylvania State University, Shanghai Astronomical Observatory, United Kingdom Participation Group, Universidad Nacional Autónoma de México, University of Arizona,University of Colorado Boulder, University of Oxford, University of Portsmouth, University of Utah, University of Virginia, University ofWashington, University of Wisconsin, Vanderbilt University, and Yale University.

[4] http://sdss-marvin.readthedocs.io/en/stable/

REFERENCES

Accurso G., et al., 2017, Monthly Notices of the Royal Astronomical Society, 470, 4750
Alban M., Wylezalek D., et al. 2022, in prep.
Avery C. R., et al., 2021, MNRAS, 503, 5134
Baker W. M., Maiolino R., et al. 2022, in prep.
Baldwin J. A., Phillips M. M., Terlevich R., 1981, Publications of the Astronomical Society of the Pacific, 93, 5
Barrera-Ballesteros J. K., et al., 2016, MNRAS, 463, 2513
Bertemes C., Wuyts S., et al. 2022, in prep.
Blanton M. R., Kazin E., Muna D., Weaver B. A., Price-Whelan A., 2011, The Astrophysical Journal, 142, 31
Blanton M. R., et al., 2017, The Astrophysical Journal, 154, 28
Bluck A. F. L., et al., 2020, MNRAS, 499, 230
Bolatto A. D., et al., 2017, ApJ, 846, 159
Brinchmann J., Charlot S., White S., Tremonti C., Kauffmann G., Heckman T., Brinkmann J., 2004, Monthly Notices of the Royal Astronomical Society, 351, 1151
Bruzual G., Charlot S., 2003, Monthly Notices of the Royal Astronomical Society, 344, 1000
Bundy K., et al., 2015, The Astrophysical Journal, 798, 7
Calzetti D., Armus L., Bohlin R. C., Kinney A. L., Koornneef J., Storchi-Bergmann T., 2000, The Astrophysical Journal, 533, 682
Carnall A. C., McLure R. J., Dunlop J. S., Davé R., 2018, Monthly Notices of the Royal Astronomical Society, 480, 4379
Carnall A. C., et al., 2019, Monthly Notices of the Royal Astronomical Society, 490, 417
Chauke P., et al., 2019, ApJ, 877, 48
Cherinka B., et al., 2019, AJ, 158, 74
Chisholm J., Tremonti C., Leitherer C., 2018, MNRAS, 481, 1690
Colombo D., et al., 2020, A&A, 644, A97
Comerford J. M., et al., 2020, ApJ, 901, 159
Ellison S. L., Patton D. R., Simard L., McConnachie A. W., 2008, ApJ, 672, L107
Ellison S. L., Thorp M. D., Pan H.-A., Lin L., Scudder J. M., Bluck A. F. L., Sánchez S. F., Sargent M., 2020, MNRAS, 492, 6027
Falcón-Barroso J., Sánchez-Blázquez P., Vazdekis A., Ricciardelli E.,

Cardiel N., Cenarro A. J., Gorgas J., Peletier R. F., 2011, A&A, 532, A95
Ferland G. J., Korista K. T., Verner D. A., Ferguson J. W., Kingdon J. B., Verner E. M., 1998, PASP, 110, 761
Gibson B. K., Pilkington K., Brook C. B., Stinson G. S., Bailin J., 2013, A&A, 554, A47
Hemler Z. S., et al., 2021, MNRAS, 506, 3024
Janowiecki S., Catinella B., Cortese L., Saintonge A., Wang J., 2020, MNRAS, 493, 1982
Kauffmann G., et al., 2003, Monthly Notices of the Royal Astronomical Society, 346, 1055
Kennicutt R. C., 1998, The Astrophysical Journal, 498, 541
Kewley L. J., Dopita M. A., Sutherland R. S., Heisler C. A., Trevena J., 2001, ApJ, 556, 121
Kewley L. J., Nicholls D. C., Sutherland R. S., 2019, ARA&A, 57, 511
Kroupa P., Boily C. M., 2002, Monthly Notices of the Royal Astronomical Society, 336, 1188
Kumari N., Maiolino R., Belfiore F., Curti M., 2019, MNRAS, 485, 367
Law D. R., et al., 2015, The Astrophysical Journal, 150, 19
Leja J., Carnall A. C., Johnson B. D., Conroy C., Speagle J. S., 2019, The Astrophysical Journal, 876, 3
Lin L., et al., 2020, ApJ, 903, 145
Lin L., et al., 2022, arXiv e-prints, p. arXiv:2201.05318
Lotz J. M., Jonsson P., Cox T. J., Primack J. R., 2008, MNRAS, 391, 1137
Lutz K. A., et al., 2021, A&A, 649, A39
Maiolino R., Mannucci F., 2019, A&ARv, 27, 3
Maiolino R., et al., 2008, A&A, 488, 463
Mannucci F., Cresci G., Maiolino R., Marconi A., Gnerucci A., 2010, MNRAS, 408, 2115
Marino R. A., et al., 2013, A&A, 559, A114
Márquez I., Masegosa J., González-Martin O., Hernández-Garcia L., Pović M., Netzer H., Cazzoli S., del Olmo A., 2017, Frontiers in Astronomy and Space Sciences, 4, 34
Martig M., Bournaud F., Teyssier R., Dekel A., 2009, Astrophysical Journal, 707, 250
Martins L. P., González Delgado R. M., Leitherer C., Cervi~no M., Hauschildt P., 2005, MNRAS, 358, 49
Nevin R., et al., 2021, ApJ, 912, 45
Noeske K., et al., 2007, The Astrophysical Journall, 660, L43
Pettini M., Pagel B., 2004, Monthly Notices of the Royal Astronomical Society, 348, L59
Piotrowska J. M., Bluck A. F. L., Maiolino R., Peng Y., 2021, MNRAS,
Renzini A., Peng Y.-j., 2015, The Astrophysical Journall, 801, L29
Rich J. A., Torrey P., Kewley L. J., Dopita M. A., Rupke D. S. N., 2012, ApJ, 753, 5
Rupke D. S. N., Kewley L. J., Chien L. H., 2010, ApJ, 723, 1255
Saintonge A., Catinella B., 2022, arXiv e-prints, p. arXiv:2202.00690
Saintonge A., et al., 2017, The Astrophysical Journals, 233, 22
Salim S., 2014, Serbian Astronomical Journal, 1, 1
Sánchez Almeida J., Sánchez-Menguiano L., 2019, ApJ, 878, L6
Sánchez-Blázquez P., et al., 2006, MNRAS, 371, 703
Sánchez S. F., et al., 2016, Rev. Mex. Astron. Astrofis., 52, 171
Sánchez S. F., et al., 2017, MNRAS, 469, 2121
Sánchez S. F., et al., 2018, Rev. Mex. Astron. Astrofis., 54, 217
Schaefer A. L., et al., 2019, ApJ, 884, 156
Schawinski K., Koss M., Berney S., Sartori L. F., 2015, MNRAS, 451, 2517
Schmidt M., 1959, The Astrophysical Journal, 129, 243
Sharda P., Wisnioski E., Krumholz M. R., Federrath C., 2021, MNRAS, 506, 1295
Simons R. C., et al., 2021, ApJ, 923, 203
Singh R., et al., 2013, A&A, 558, A43
Smee S. A., et al., 2013, The Astrophysical Journal, 146, 32
Stinson G. S., Bailin J., Couchman H., Wadsley J., Shen S., Nickerson S., Brook C., Quinn T., 2010, MNRAS, 408, 812
Thorp M. D., Ellison S. L., Simard L., Sánchez S. F., Antonio B., 2019, MNRAS, 482, L55
Tremonti C. A., et al., 2004, ApJ, 613, 898
Vale Asari N., Couto G. S., Cid Fernandes R., Stasińska G., de Amorim A. L., Ruschel-Dutra D., Werle A., Florido T. Z., 2019, MNRAS, 489, 4721
Vazdekis A., Sánchez-Blázquez P., Falcón-Barroso J., Cenarro A. J., Beasley M. A., Cardiel N., Gorgas J., Peletier R. F., 2010, MNRAS, 404, 1639
Veilleux S., Cecil G., Bland-Hawthorn J., 2005, ARA&A, 43, 769
Wake D. A., et al., 2017, The Astrophysical Journal, 154, 86
Wylezalek D., Flores A. M., Zakamska N. L., Greene J. E., Riffel R. A., 2020, MNRAS, 492, 4680
Wylezalek D., et al., 2022, MNRAS, 510, 3119
Yan R., et al., 2016a, The Astrophysical Journal, 151, 8
Yan R., et al., 2016b, The Astrophysical Journal, 152, 197
Zhang K., et al., 2017, Monthly Notices of the Royal Astronomical Society, 466, 3217

APPENDIX A: DISCARDING POTENTIAL POST-MERGER SYSTEMS

In this Section, we briefly check that our results do not strongly depend on the inclusion of galaxies with potential post-merger signatures. As discussed in Section 4.4, we visually inspected the Hα, [O III] λ5007 and stellar velocity maps to search for kinematic misalignements between the stellar and gas-phase components as a potential sign of post-merger status. The maps were produced with `Marvin` (Cherinka et al. 2019) using Voronoi binning with a S/N cutoff of 3. Fig A1 shows the $\nabla Z - t_{\rm dep}$ relation that we obtain when excluding the galaxies with the following Plate-IFUs: 8588-6101, 8595-3703, 8084-6103. The relation remains robust. In Fig A2, we further show that the relation between ∇Z and the [O III] line width within 1 R_e remains significant when excluding those objects.

For reference, we provide the kinematic maps used for this exercise in Fig A3.

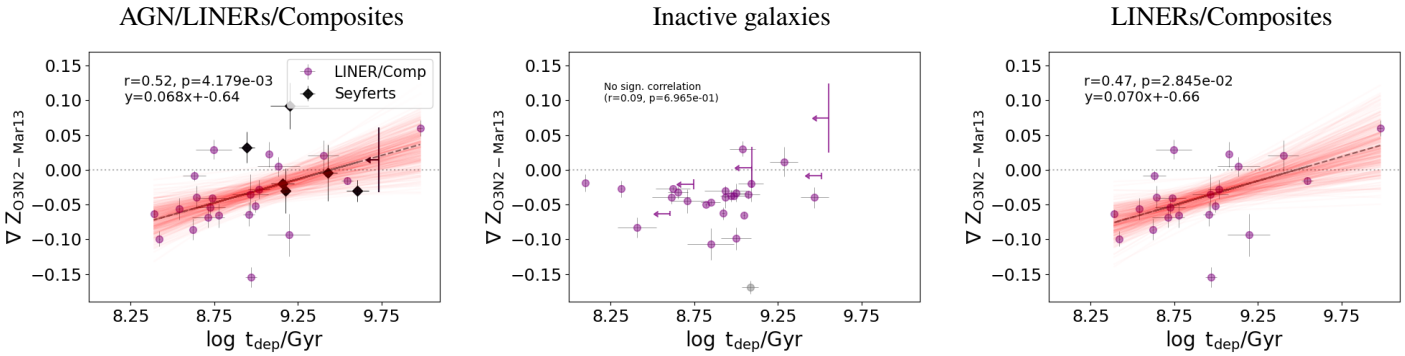

Figure A1. Same as Fig 2, but excluding objects which show potential evidence for a mis-alignement between their stellar and gas-phase kinematics.

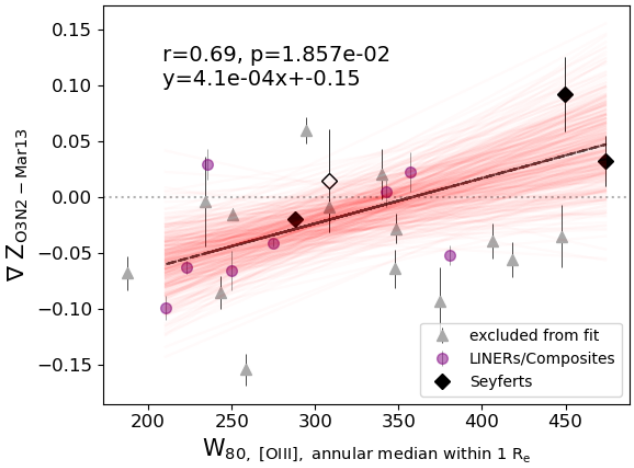

Figure A2. Same as Fig 8, but excluding objects which show potential evidence for a mis-alignement between their stellar and gas-phase kinematics.

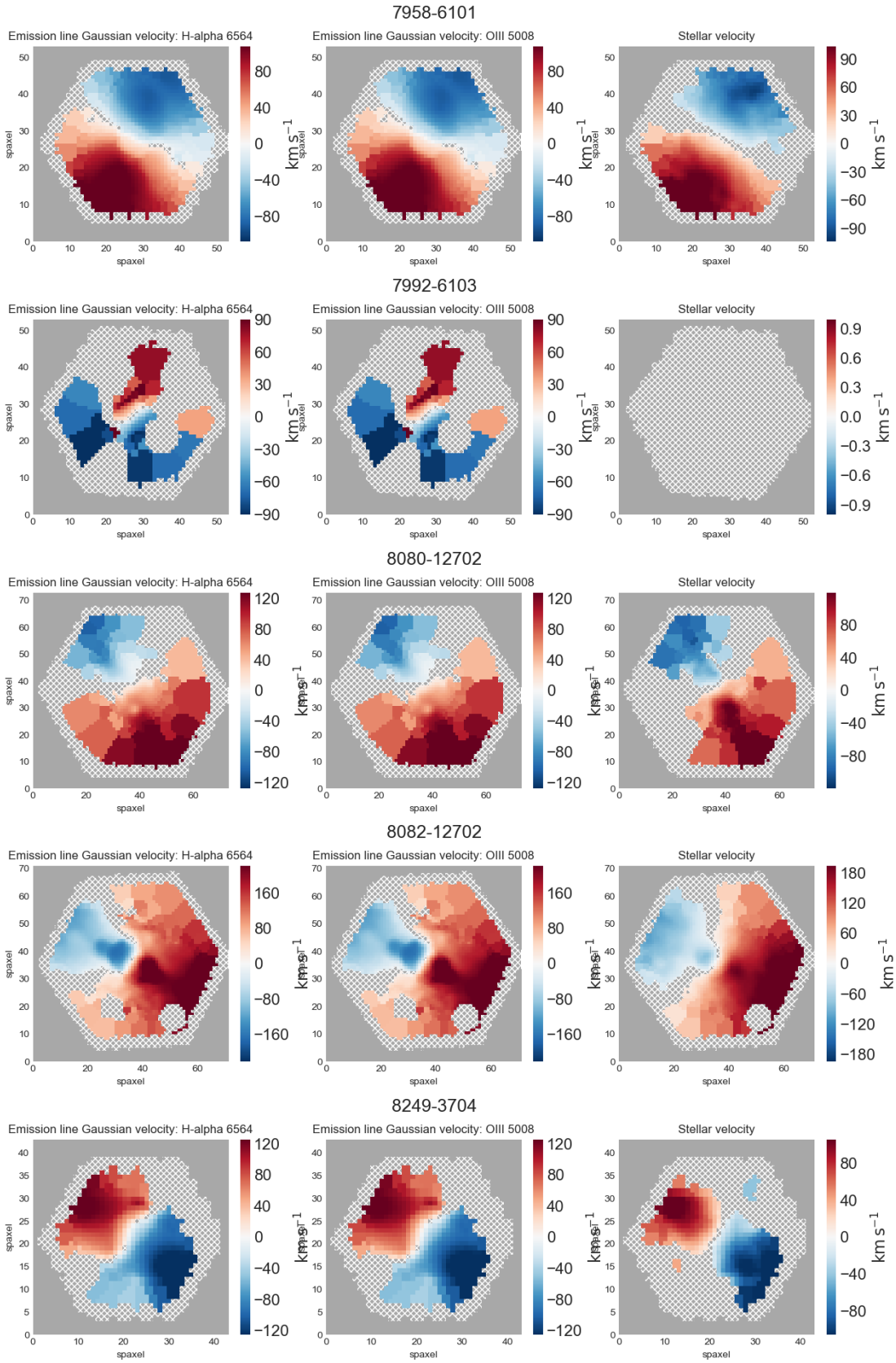

Figure A3. Velocity maps for the AGN, LINERs and Composites in our sample. *Left panel*: Hα velocity field. *Middle panel*: [O III] λ5007 velocity field. *Right panel*: Stellar velocity field.

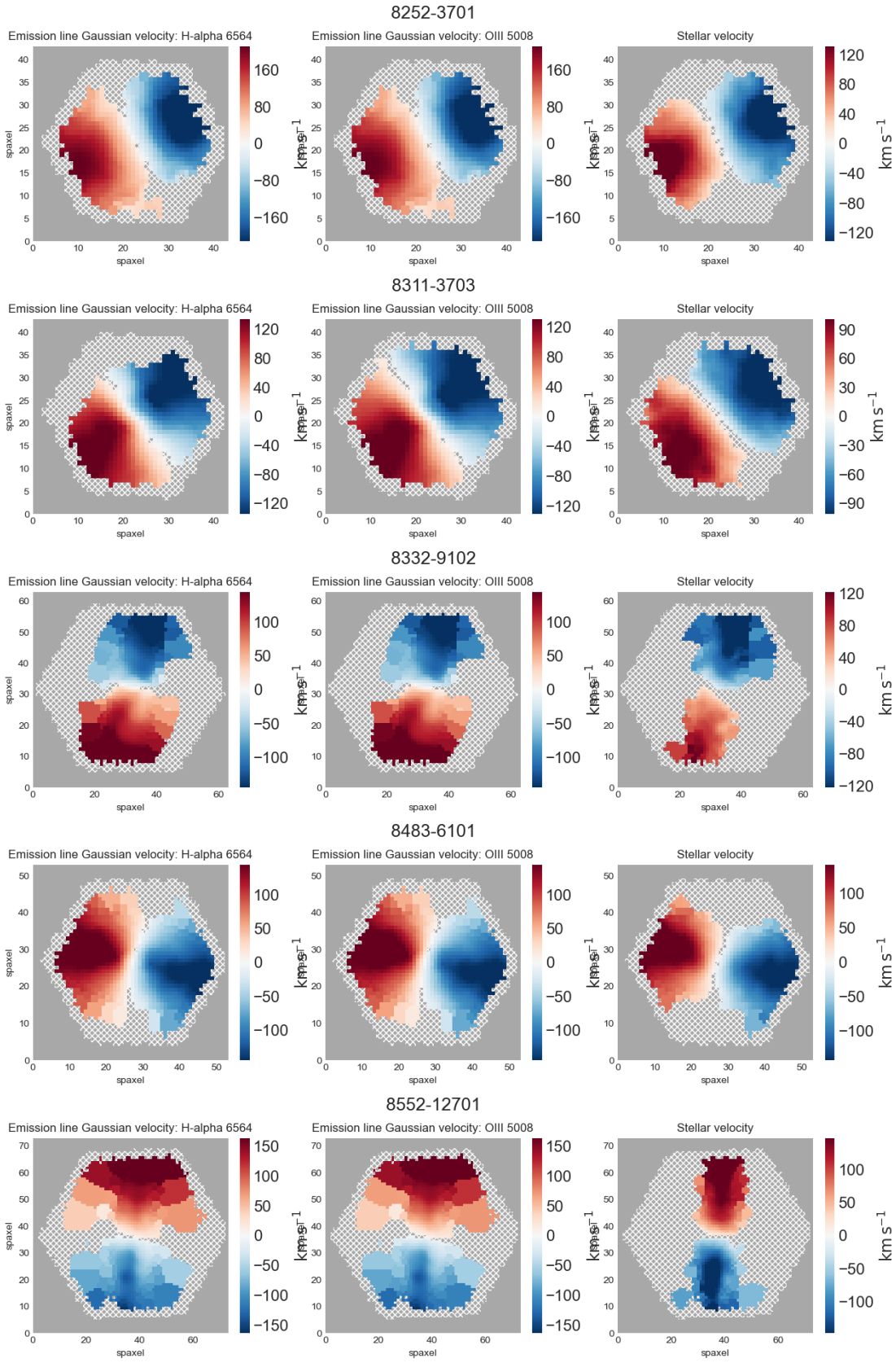

Figure A3. (cont.)

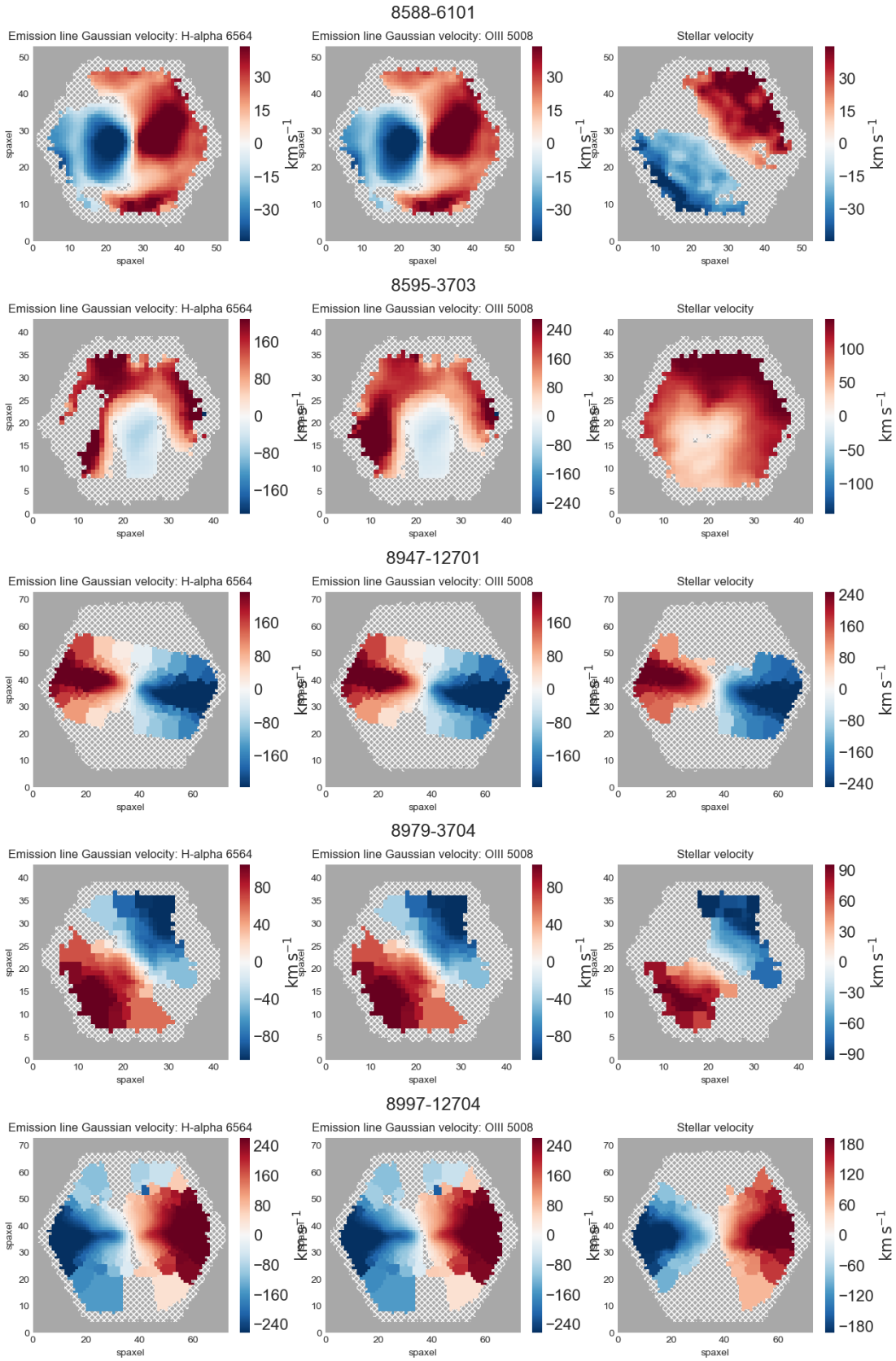

Figure A3. (cont.)

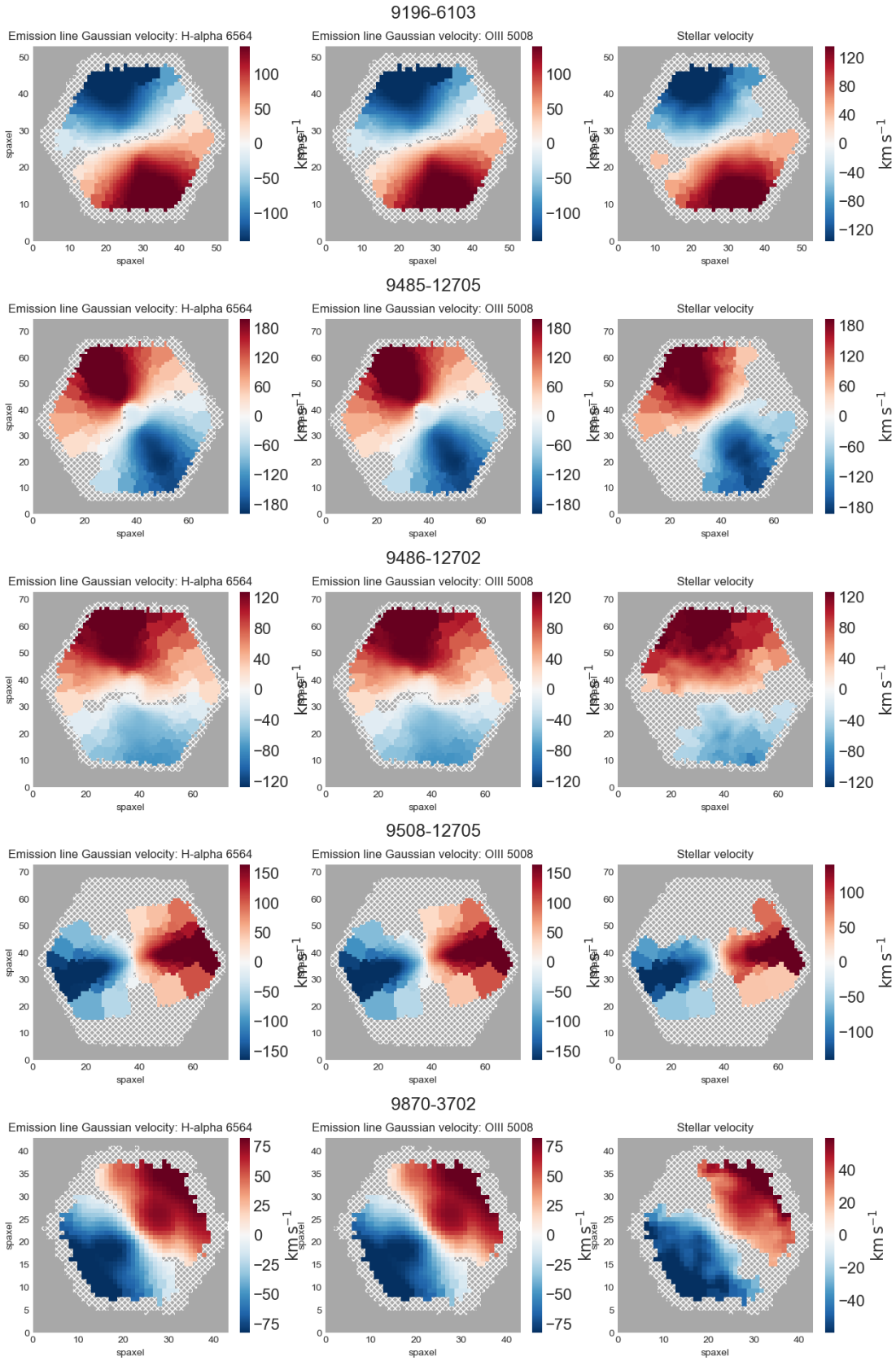

Figure A3. (cont.)

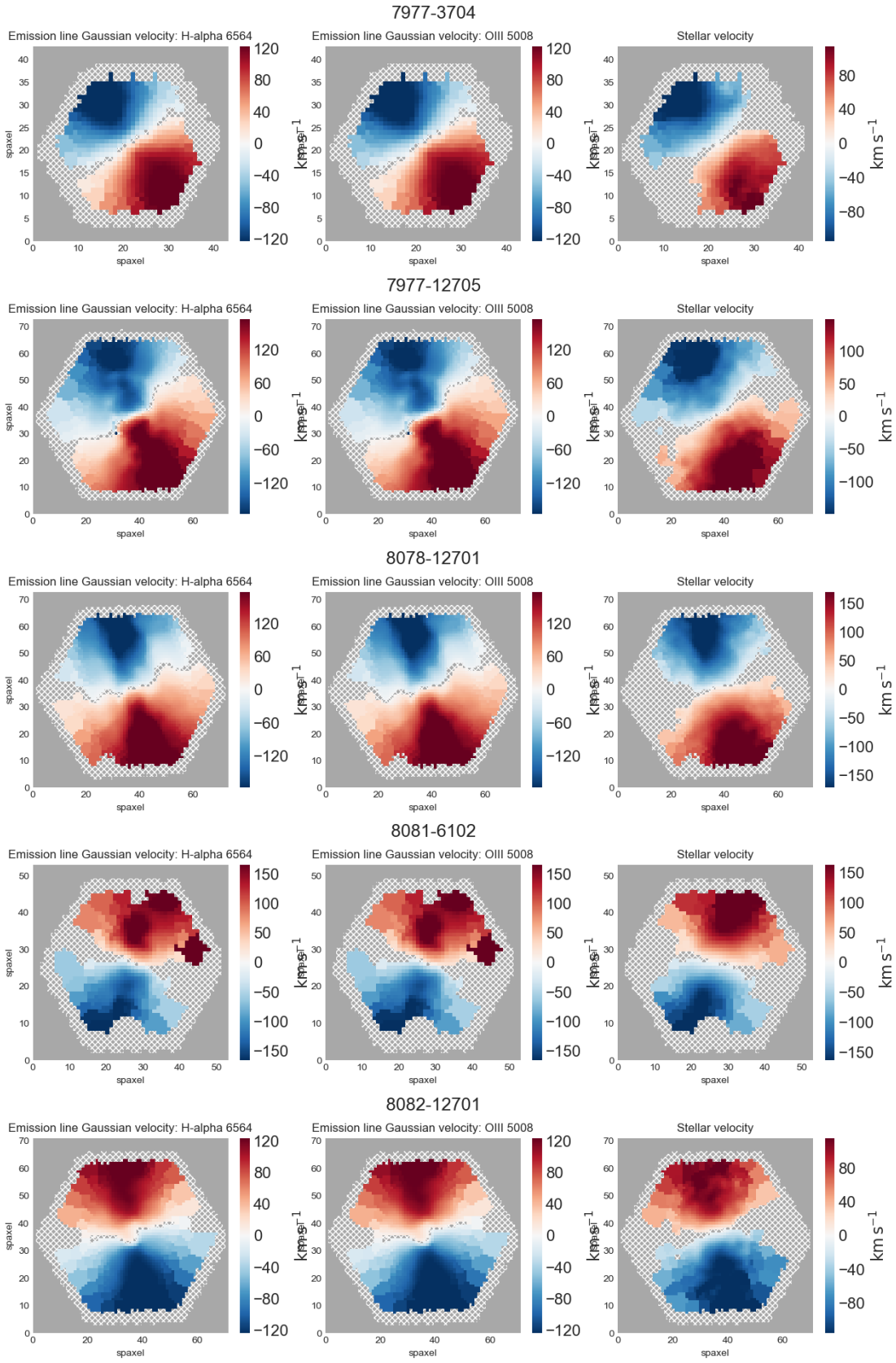

Figure A3. (cont.)

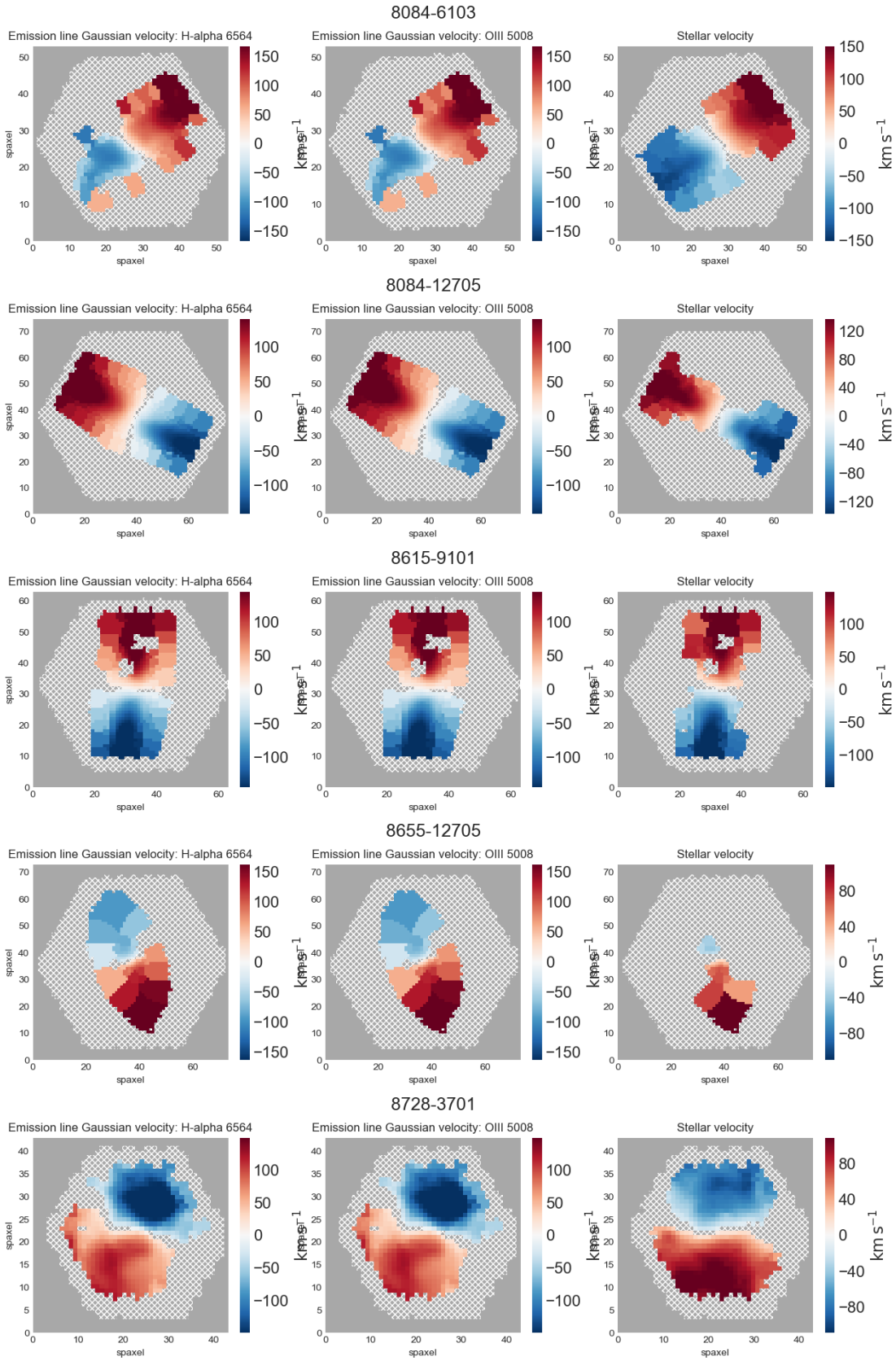

Figure A3. (cont.)

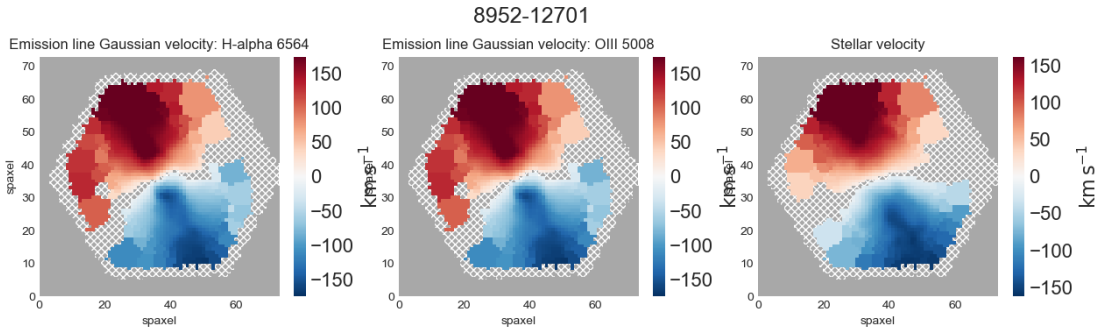

Figure A3. (cont.)